

Physical and Chemical Characterization of GY 91's Multi-ringed Protostellar Disk with ALMA

SALLY D. JIANG , JANE HUANG , IAN CZEKALA , LEON TRAPMAN , YURI AIKAWA , SEAN M. ANDREWS ,⁵
 JAEHAN BAE ,⁶ EDWIN A. BERGIN , CHARLES J. LAW ,^{8,*} ROMANE LE GAL ,^{9,10} FENG LONG ,^{11,12,*}
 FRANÇOIS MÉNARD ,¹³ KARIN I. ÖBERG , CHUNHUA QI ,¹⁴ RICHARD TEAGUE ,¹⁵ DAVID J. WILNER ,⁵ AND
 KE ZHANG 

¹Department of Astronomy, Columbia University, 538 W. 120th Street, Pupin Hall, New York, NY 10027, USA

²School of Physics & Astronomy, University of St. Andrews, North Haugh, St. Andrews KY16 9SS, UK

³Department of Astronomy, University of Wisconsin-Madison, 475 N Charter St, Madison, WI 53706

⁴Department of Astronomy, Graduate School of Science, The University of Tokyo, 7-3-1 Hongo, Bunkyo-ku, Tokyo 113-0033, Japan

⁵Center for Astrophysics | Harvard & Smithsonian, 60 Garden Street, Cambridge, MA 02138, USA

⁶Department of Astronomy, University of Florida, Gainesville, FL 32611, USA

⁷Department of Astronomy, University of Michigan, 323 West Hall, 1085 S. University Avenue, Ann Arbor, MI 48109, USA

⁸Department of Astronomy, University of Virginia, Charlottesville, VA 22904, USA

⁹Université Grenoble Alpes, CNRS, IPAG, F-38000 Grenoble, France

¹⁰Institut de Radioastronomie Millimétrique (IRAM), 300 rue de la piscine, F-38406 Saint-Martin d'Hères, France

¹¹Kavli Institute for Astronomy and Astrophysics, Peking University, Beijing 100871, China

¹²Lunar and Planetary Laboratory, University of Arizona, Tucson, AZ 85721, USA

¹³Univ. Grenoble Alpes, CNRS, IPAG, 38000 Grenoble, France

¹⁴Institute for Astrophysical Research, Boston University, 725 Commonwealth Avenue, Boston, MA 02215, USA

¹⁵Department of Earth, Atmospheric, and Planetary Sciences, Massachusetts Institute of Technology, Cambridge, MA 02139, USA

ABSTRACT

GY 91, commonly categorized as a Class I young stellar object, is notable for disk dust substructures that have been hypothesized to trace early planet formation. Using the ALMA 12-m and ACA arrays, we present new Band 7 dust continuum and molecular line observations of GY 91 at an angular resolution of $\sim 0.3''$ (40 au). We report detections of CS $J = 6 - 5$, N₂H⁺ $J = 3 - 2$, C¹⁸O $J = 3 - 2$, H₂CS $J_{K_a, K_c} = 8_{1,7} - 7_{1,6}$, H₂CO $J_{K_a, K_c} = 4_{0,4} - 3_{0,3}$, and H₂CO $J_{K_a, K_c} = 4_{2,3} - 3_{2,2}$, as well as a tentative detection of ¹³C¹⁸O $J = 3 - 2$. We observe azimuthal asymmetry in CS and H₂CS emission, as well as radially structured H₂CO $4_{0,4} - 3_{0,3}$ emission outside the dust continuum. C¹⁸O and H₂CO $4_{0,4} - 3_{0,3}$ show significant cloud contamination, while CS and N₂H⁺ are good tracers of Keplerian rotation originating from the disk. Envelope emission does not appear to contribute significantly either to the continuum or molecular line observations. GY 91's chemical properties appear in large part to resemble those of Class II disks, although observations of additional molecular probes should be obtained for a fuller comparison. With CS, we estimated a dynamical stellar mass of $0.58 M_{\odot}$, which is higher than previous estimates from stellar evolutionary models ($0.25 M_{\odot}$). Using both radiative transfer modeling of the dust continuum and comparison of the C¹⁸O and N₂H⁺ fluxes to literature thermochemical models, we estimate a disk mass of $\sim 0.01 M_{\odot}$.

1. INTRODUCTION

High-resolution millimeter/sub-millimeter continuum observations have resulted in an updated view of protoplanetary disk evolution. Class II disks show diverse and nearly ubiquitous dust substructures such as rings, gaps, and spirals (e.g., Andrews et al. 2018; Long et al. 2018; Cieza et al. 2019). While the exact origins of

these substructures are contested, theories have pointed to processes such as planet-disk interactions (e.g., Goldreich & Tremaine 1980; Zhang et al. 2018; Baruteau et al. 2014; Paardekooper et al. 2023), magnetic disk winds (e.g., Suriano et al. 2018), dust evolution related to snowline locations (e.g., Zhang et al. 2015), or secular gravitational instability (Takahashi & Inutsuka 2014). Meanwhile, the prevalence of dust substructures in younger Class I disks is less clear. While the eDisk survey (Ohashi et al. 2023) found that few disks in their sample showed clear substructure, Hsieh et al. (2025)

Email: sj3323@columbia.edu, jane.huang@columbia.edu

* NASA Hubble Fellowship Program Sagan Fellow

and [Vioque et al. \(2025\)](#) report high detection rates in Class I disks. This difference may be due to the star-forming regions targeted or to the eDisk sample skewing younger than the other samples. If these substructures are due to planet-disk interactions, detections in Class I disks may place constraints on the timescales of planet formation and would suggest that giant planets are assembled faster than previously thought, in under 1 Myr (e.g., [Sheehan & Eisner 2018](#); [Segura-Cox et al. 2020](#)). Alternatively, these substructures could represent sites that are favorable for future planet formation due to high concentrations of solids (e.g., [Morbidelli 2020](#)). In either case, studies of Class I disks with substructures can provide a window into an important transitional point in disk evolution.

The young stellar object (YSO) GY 91 (also known as ISO-Oph 54) is well-known for its disk substructures and has commonly been categorized as Class I based on its bolometric temperature (372 K) and mid-IR SED slope ($\alpha_{IR} = 0.45$) ([Enoch et al. 2009](#); [Sheehan & Eisner 2018](#)). It is located in the Rho Ophiuchi cloud complex, which is at a distance of 140 parsecs ([Cánovas et al. 2019](#)). GY 91 itself does not have a parallax measurement from *Gaia* ([Gaia Collaboration et al. 2016, 2021](#)) due to high extinction ($A_V = 53$, [Cieza et al. \(2021\)](#)). The millimeter continuum disk consists of at least 4 pairs of axisymmetric rings and gaps ([Sheehan & Eisner 2018](#); [Cieza et al. 2021](#)). From radiative transfer modeling of the SED and millimeter continuum, [Sheehan & Eisner \(2018\)](#) estimated an envelope-to-disk mass ratio of ~ 0.12 and an age of 0.5 Myr. However, [McClure et al. \(2010\)](#) argued that GY 91 should more appropriately be categorized as an envelope-free Class II YSO with a high amount of foreground cloud material being responsible for the infrared excess mimicking an envelope contribution. [van Kempen et al. \(2007\)](#) also classified GY 91 as an envelope-free source based on a single-dish HCO^+ survey of YSOs.

Most of the published ALMA observations of GY 91 so far have been high-resolution continuum observations, which resolve out larger-scale emission ([Hsieh et al. 2024](#); [Sheehan & Eisner 2018](#); [Cieza et al. 2021](#)). The only spatially resolved molecular line observations published to date have been of ^{12}CO $J = 2 - 1$ with a synthesized beam size of $0''.13$ (18 au) and maximum recoverable scale of $0''.67$ (95 au), while the gas disk extends past a radius of 100 au ([Antilen et al. 2023](#)). [Antilen et al. \(2023\)](#) noted the presence of significant cloud emission in ^{12}CO , with disk emission only being detected via the Keplerian line wings that trace smaller radii.

To investigate the physical and chemical properties of GY 91 further, we obtained new ALMA molecular line and dust continuum observations of GY 91 using multiple antenna configurations in order to be sensitive to emission on both disk and envelope scales. We targeted a suite of molecular lines, including common bright disk gas tracers such as C^{18}O , N_2H^+ , CS, and H_2CO (e.g., [Anderson et al. 2019](#); [Le Gal et al. 2019](#); [Pegues et al. 2020](#); [Öberg et al. 2021](#)), in order to study the structure, kinematics, and chemistry of the gas around GY 91. Because the high foreground extinction poses a challenge to observing GY 91, we targeted transitions with upper state energy levels > 25 K with the aim of preferentially tracing the warmer disk gas over colder foreground cloud material.

We describe the observational setup and data reduction process in [Section 2](#), provide an overview of line detections and spatial distributions in [Section 3](#), estimate the dynamical stellar mass in [Section 4](#), gauge envelope contributions to the observed emission in [Section 5](#), and estimate the disk mass in [Section 6](#). Finally, we discuss the results in [Section 7](#) and present conclusions in [Section 8](#).

2. ALMA OBSERVATIONS AND DATA REDUCTION

Observations of GY 91 were taken in ALMA Project 2021.1.01588.S (P.I.: J. Huang) in Cycle 8. In order to maintain sensitivity to larger-scale envelope emission while still spatially resolving the disk, GY 91 was targeted using two 12-m antenna configurations (which we refer to as “compact” for the one with shorter maximum baselines and “extended” for the one with longer maximum baselines) and the 7-meter Atacama Compact Array (ACA). Further information about the observational setup is shown in [Table 1](#). Two Band 7 spectral settings were used, covering both the continuum and the following seven lines: CS $J = 6 - 5$, $\text{N}_2\text{H}^+ J = 3 - 2$, $\text{H}_2\text{CS} J_{K_a, K_c} = 8_{1,7} - 7_{1,6}$, $\text{H}_2\text{CO} J_{K_a, K_c} = 4_{0,4} - 3_{0,3}$, $\text{H}_2\text{CO} J_{K_a, K_c} = 4_{2,3} - 3_{2,2}$, $\text{C}^{18}\text{O} J = 3 - 2$, and $^{13}\text{C}^{18}\text{O} J = 3 - 2$. We refer to the lower frequency setting as “7a” and the higher frequency setting as “7b.” The maximum recoverable scale (MRS)¹⁶ is $7''.3$ (1020 au) for setting 7a and $7''.2$ (1010 au) for 7b. The spectral setup is explained in more detail in [Table 2](#).

Initial calibration of all data was performed by NAASC (North American ALMA Science Center) staff using the CASA 6.2 pipeline ([CASA Team et al. 2022](#)).

¹⁶ Defined by the ALMA Technical Handbook to be $\frac{0.983\lambda}{L_5}$, where λ is the observing wavelength and L_5 is the 5th percentile baseline length

Table 1. Observational Setup for GY 91

Spectral Setting	Obs Date	Antenna Count	Baselines (m)	Time on target (min)	Flux/Bandpass Calibrator	Phase Calibrator
7a	2022 March 10	43 (12-m)	15-284	18	J1517-2422	J1625-2527
	2022 April 24	10 (ACA 7-m)	8.9-45	42	J1924-2914	J1700-2610
	2022 April 25	10 (ACA 7-m)	8.9-45	42	J1924-2914	J1700-2610
	2022 June 14	42 (12-m)	15.1-1300	26	J1517-2422	J1700-2610
	2022 June 30	46 (12-m)	15.1-1300	26	J1517-2422	J1700-2610
7b	2022 March 08	42 (12-m)	15-284	33	J1517-2422	J1625-2527
	2022 March 27	8 (ACA 7-m)	8.9-45	47	J1924-2914	J1700-2610
	2022 April 19	10 (ACA 7-m)	8.9-45	47	J1924-2914	J1700-2610
	2022 April 22	10 (ACA 7-m)	8.9-45	47	J1924-2914	J1700-2610
	2022 April 23	10 (ACA 7-m)	8.9-45	47	J1924-2914	J1700-2610
	2022 June 10	42 (12-m)	15.1-1200	49	J1517-2422	J1700-2610
	2022 June 11	43 (12-m)	15.1-1200	49	J1517-2422	J1700-2610

Table 2. Spectral Window Setup

Spectral Setting	Targeted Line	E_u (K)	Rest Frequency* (GHz)	Resolution (MHz)	Bandwidth (MHz)	Channel Number
7a	$\text{H}_2\text{CS } J_{K_a, K_c} = 8_{1,7} - 7_{1,6}$ (ortho)	73.4	278.8876613	0.141	117.19-125	960 - 1024
	$\text{N}_2\text{H}^+ J = 3 - 2$	26.8	279.5117491	0.141	117.19-125	960 - 1024
	$\text{H}_2\text{CO } J_{K_a, K_c} = 4_{0,4} - 3_{0,3}$ (para)	34.9	290.623405	0.141	117.19-125	960 - 1024
	$\text{H}_2\text{CO } J_{K_a, K_c} = 4_{2,3} - 3_{2,2}$ (para)	82.1	291.2377664	0.141	117.19-125	960 - 1024
	CS $J = 6 - 5$	49.4	293.9120865	0.141	234.38-250	1920 - 2048
	Continuum		281	31.25	2000	128
7b	$^{13}\text{C}^{18}\text{O } J = 3 - 2$	30.2	314.11964530	0.141	234.38-250	1920 - 2048
	$\text{C}^{18}\text{O } J = 3 - 2$	31.6	329.33055250	0.141	234.38-250	1920 - 2048
	Continuum		316	31.25	2000	128
	Continuum		328.2	31.25	2000	128

NOTE—*Rest frequencies and E_u obtained from the Cologne Database for Molecular Spectroscopy (CDMS) (Müller et al. 2001, 2005; Endres et al. 2016)

Further self-calibration and imaging were completed using CASA 6.5. We first flagged all channels where line emission was expected to be present and created spectrally averaged continuum measurement sets for each spectral setting. The continuum from each execution was then imaged using the `tclean` algorithm with Briggs weighting and a `robust` value of 0.5, using the Hogbom deconvolver for the ACA and compact 12-m observations and the multiscale deconvolver for the extended 12-m observations. To correct for slight (sub-beam) positional offsets between observations from different configurations, we followed the procedure described in Andrews et al. (2018). We fit a Gaussian to the continuum to measure the position of the disk centers, applied phase shifts to move the disk center to the phase cen-

ter, and then relabeled the phase centers to match the coordinates of one of the 12-m extended configuration execution block’s phase center. The measurement sets were then reimaged and manually checked to ensure the centers were properly aligned. Finally, the measurement sets for the different configurations were concatenated to create a combined set of continuum visibilities for each spectral setting.

Self-calibration and imaging processes were then performed separately for the two spectral settings. Two iterations of phase-only self-calibration were performed, first with a scan-length solution interval and then with a 120 s interval. Amplitude calibration was conducted once with a scan-length solution interval. The final continuum image for each spectral setting was produced

using multiscale CLEAN with scales of [0'', 0''2, 0''4, 1''] and a `robust` value of 0.5.

We then applied the gain tables from the phase and amplitude self-calibration of the continuum to the line spectral windows. The continuum was fit with a first-order polynomial and subtracted from the spectral windows using `uvcontsub`. Line images were produced with `tclean` using the multiscale deconvolver and the `AUTO-MULTITHRESH` auto-masking algorithm (Kepley et al. 2020) to create masks for the irregularly-shaped line emission. The automasking parameters were motivated by NRAO’s CASA Guide-recommended values.¹⁷ To improve the signal-to-noise (S/N) of the weaker lines (H_2CS , N_2H^+ , both H_2CO transitions, and $^{13}\text{C}^{18}\text{O}$), a 0''2 *uv*-taper was applied in `tclean`. This procedure multiplies the weights by a 2D Gaussian with a user-specified FWHM, thereby downweighting data at longer baselines, increasing surface brightness sensitivity, and degrading the angular resolution (Briggs 1995). Finally, all images were primary beam-corrected. The image properties are summarized in Table 3. ¹⁸

3. MOLECULAR LINE CHARACTERIZATION

3.1. *Image overview*

We present the individual channel maps for each line in Appendix A. Matched filtering was used to quantify the significance of line detection (see Appendix B). The 1.05 mm continuum image and integrated intensity maps (zeroth-moment maps) for the molecular lines are shown in Figure 1. Although high-resolution ALMA images ($< 0''.13$) have shown that the GY 91 disk has multiple dust gaps (Sheehan & Eisner 2018; Cieza et al. 2021), our new continuum image appears mostly smooth due to our lower resolution ($\sim 0''.3$). The integrated intensity maps were created for most lines by collapsing the image cube from 1 to 7 km s^{-1} , which represents the velocity range over which CS (the strongest line without significant foreground contamination) is detected above the 3σ level. C^{18}O was integrated over a slightly wider velocity range (0 to 7.5 km s^{-1}). Cloud contamination is visible in the channel maps (Appendix A) for both C^{18}O ($2.5 \text{ km s}^{-1} < v_{lsrk} < 3.75 \text{ km s}^{-1}$) and H_2CO $4_{0,4} - 3_{0,3}$ ($2.75 \text{ km s}^{-1} < v_{lsrk} < 3.5 \text{ km s}^{-1}$). To address this, a Keplerian mask was used to limit the zeroth-moment computation to the spatial regions where disk emission is expected. The mask was generated with the `keplerian_mask` software (Teague 2020) using the

inclination ($36^\circ.4$) and position angle ($157^\circ.6$) constrained from parametric modeling of the high-resolution millimeter continuum in Appendix C, and the stellar mass ($0.58 M_*$) and systemic velocity (3.87 km s^{-1}) obtained from modeling the CS kinematics in Section 4, respectively. We used a radius of $2''$ for the Keplerian mask and convolved it with a Gaussian with the same size as the synthesized beam.

In the C^{18}O and H_2CO $4_{0,4} - 3_{0,3}$ channel maps (Appendix A) and integrated intensity maps (Figure 1), the northwest side of the disk shows cloud contamination, while the southeast side exhibits minimal contamination. The integrated intensity maps for CS and H_2CS (Figure 1) show slightly asymmetric emission, with the southeast of the disk being brighter than the northwest. H_2CS does not show any evidence of large-scale non-disk emission, and CS shows only very faint large-scale emission in a couple channels ($3.25\text{--}3.5 \text{ km s}^{-1}$) of the channel maps (Appendix A), so their asymmetric emission may reflect genuine underlying azimuthal asymmetries in their column densities (see Section 7 for further commentary).

For the lines with sufficient S/N (CS, N_2H^+ , H_2CO $4_{0,4} - 3_{0,3}$, C^{18}O and H_2CS), we created intensity-weighted velocity maps (moment 1 maps) with the same velocity range as the integrated intensity maps. These moment 1 maps are shown in Figure 2. For most of these, a 5σ pixel clip was applied so that values were only calculated for strongly-detected emission. A 4σ clip was applied for H_2CS due to its lower S/N. Keplerian rotation tracing the disk is visible in the maps for CS, N_2H^+ , H_2CO $4_{0,4} - 3_{0,3}$, and C^{18}O , with the northwest side of the disk being blueshifted with respect to the systemic velocity (3.87 km s^{-1}), and the southeast side being redshifted. The H_2CO $4_{0,4} - 3_{0,3}$ and C^{18}O appear asymmetric due to foreground absorption and the presence of large-scale emission (see also Section 5), whereas CS and N_2H^+ trace the disk more cleanly. The kinematics of H_2CS are less clear due to the lower S/N, but it shows blueshifted emission to the northwest of the star and redshifted emission in the southeast, similar to the other lines. Furthermore, its compact radial extent in the integrated intensity map (Figure 1) suggests that H_2CS also likely originates predominantly in the disk.

Radial profiles for all lines and the 1.05 mm dust continuum are shown in Figure 3. The deprojected, azimuthally averaged radial profile for each line was calculated from the integrated intensity maps using `gofish` (Teague 2019a). Because the blueshifted (northwest) sides of the C^{18}O and H_2CO $4_{0,4} - 3_{0,3}$ disk emission exhibit heavy contamination, we calculated the radial profiles by creating integrated intensity maps of the red-

¹⁷ https://casaguides.nrao.edu/index.php/Automasking_Guide_CASA_6.5.4

¹⁸ The visibilities and images can be downloaded from Zenodo: <https://zenodo.org/records/17965437>

Table 3. Imaging Summary

Transition	Synthesized beam (arcsec \times arcsec, (deg))	Tapered (0''.2)	Per-channel rms ^a (mJy beam $^{-1}$)	Moment 0 rms (mJy beam $^{-1}$ km s $^{-1}$)	Flux ^c (mJy km s $^{-1}$)
$\text{H}_2\text{CS } J_{K_a, K_c} = 8_{1,7} - 7_{1,6}$	$0''.43 \times 0''.34, (-88^\circ.2)$	✓	2.0	2.5	51 ± 8
$\text{N}_2\text{H}^+ J = 3 - 2$	$0''.43 \times 0''.34 (-88.4)$	✓	2.2	3.2	282 ± 9
$\text{H}_2\text{CO } J_{K_a, K_c} = 4_{0,4} - 3_{0,3}$	$0''.42 \times 0''.34 (85^\circ.7)$	✓	2.3	3.5	322 ± 12^d
$\text{H}_2\text{CO } J_{K_a, K_c} = 4_{2,3} - 3_{2,2}$	$0''.41 \times 0''.34 (-89^\circ.9)$	✓	2.0	3.1	58 ± 8
CS $J = 6 - 5$	$0''.30 \times 0''.23 (-85^\circ.1)$	✗	1.9	3.0	768 ± 9
$^{13}\text{C}^{18}\text{O } J = 3 - 2$	$0''.46 \times 0''.36 (75^\circ.0)$	✓	1.7	2.7	17 ± 7
$\text{C}^{18}\text{O } J = 3 - 2$	$0''.37 \times 0''.24 (68^\circ.6)$	✗	2.2	4.2	696 ± 12^d
1.05 mm continuum (7a)	$0''.32 \times 0''.25 (82^\circ.6)$	✗	-	0.02^b	155.1 ± 0.2
0.93 mm continuum (7b)	$0''.37 \times 0''.24 (70^\circ.1)$	✗	-	0.03^b	223.6 ± 0.2

^aChannels have a velocity width of 0.25 km s $^{-1}$

^bContinuum rms units are in mJy beam $^{-1}$

^cError estimate do not include 10% systematic flux calibration uncertainty

^dSignificant cloud contamination

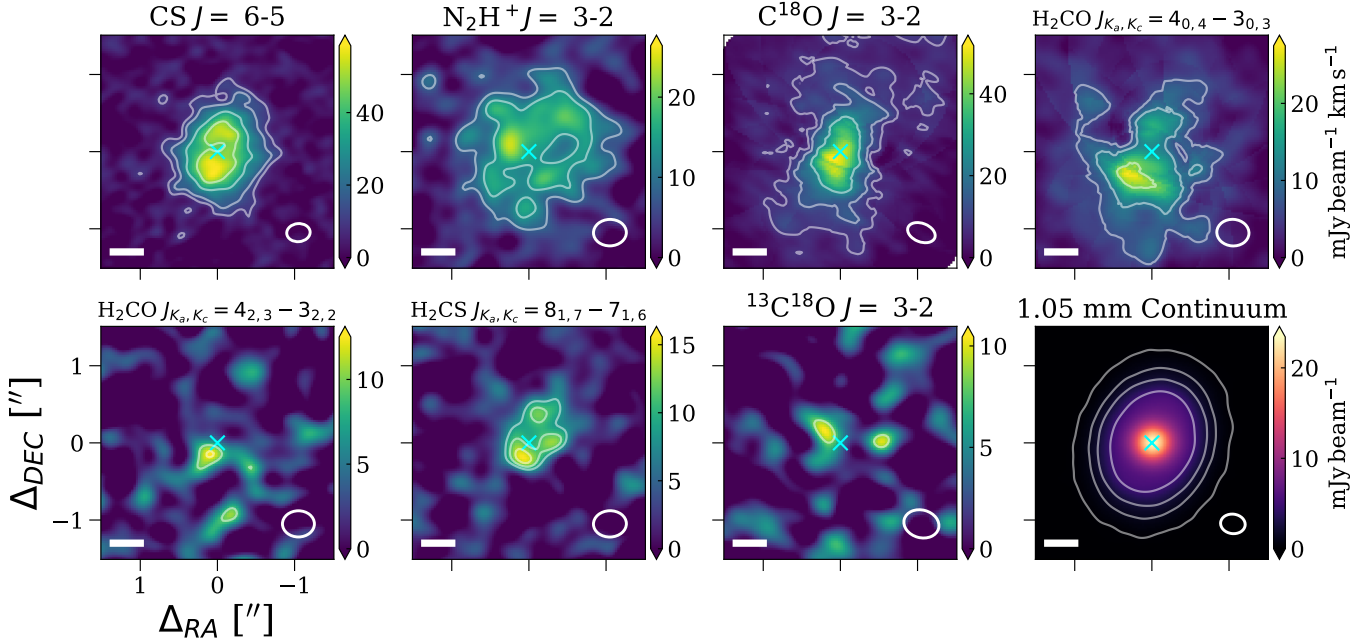


Figure 1. Zeroth moment maps of molecular line emission and the 1.05 mm dust continuum image. The synthesized beam size is indicated in the lower right of each image. CS contours are at the 3, 5, 10, and 15 σ levels, where σ is the rms listed in Table 3. The N_2H^+ , $\text{H}_2\text{CO } 4_{0,4} - 3_{0,3}$, and C^{18}O contour levels are at 3, 5, and 7 σ . H_2CS , $\text{H}_2\text{CO } 4_{2,3} - 3_{2,2}$, and $^{13}\text{C}^{18}\text{O}$ have contours at 3, 4, and 5 σ . The dust continuum contours are at 10, 50, 100, and 200 σ . A Keplerian mask was used to compute the zeroth-moment maps of $\text{H}_2\text{CO } 4_{0,4} - 3_{0,3}$ and C^{18}O . A 50 au scale bar is shown in the bottom left of each panel. The location of the continuum peak is marked with a cyan cross.

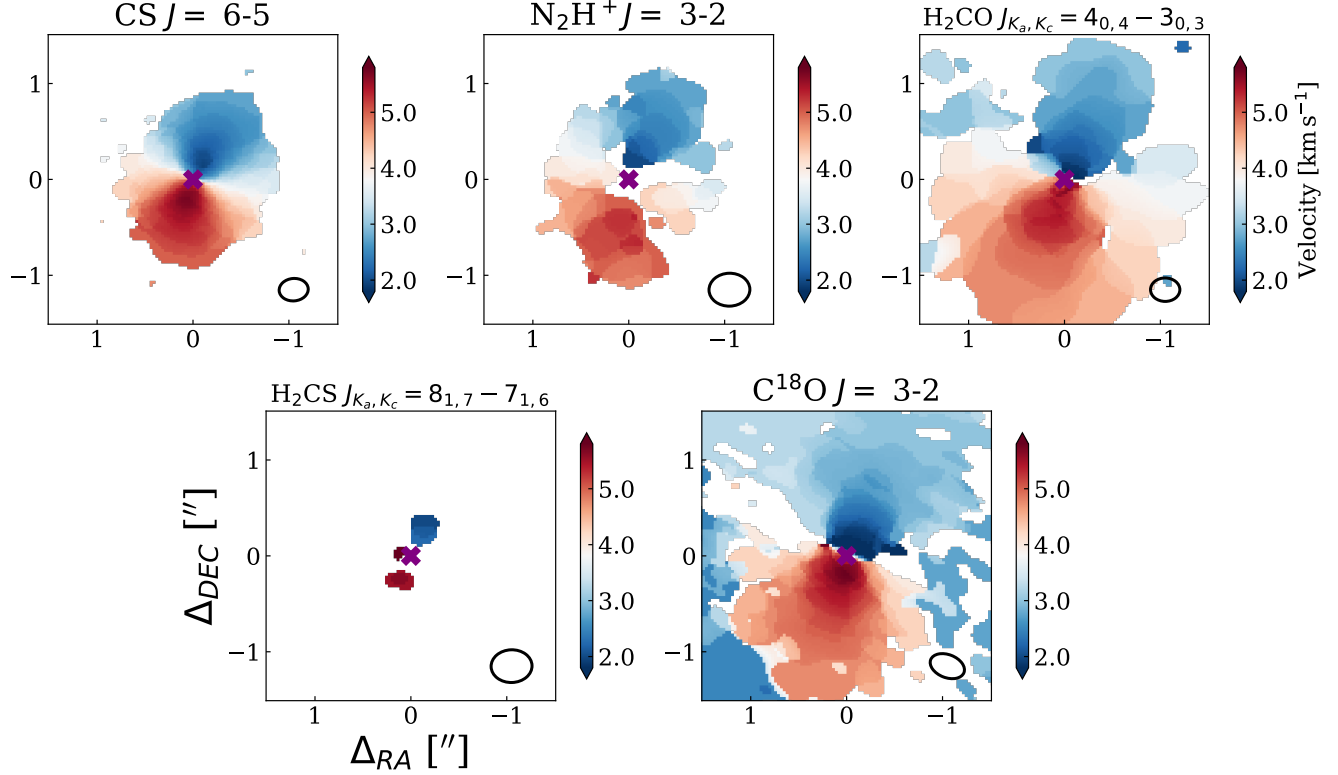


Figure 2. Moment 1 maps of CS, N_2H^+ , H_2CO $4_{0,4}-3_{0,3}$, H_2CS , and C^{18}O . The synthesized beam is shown in the lower right corner of each panel.

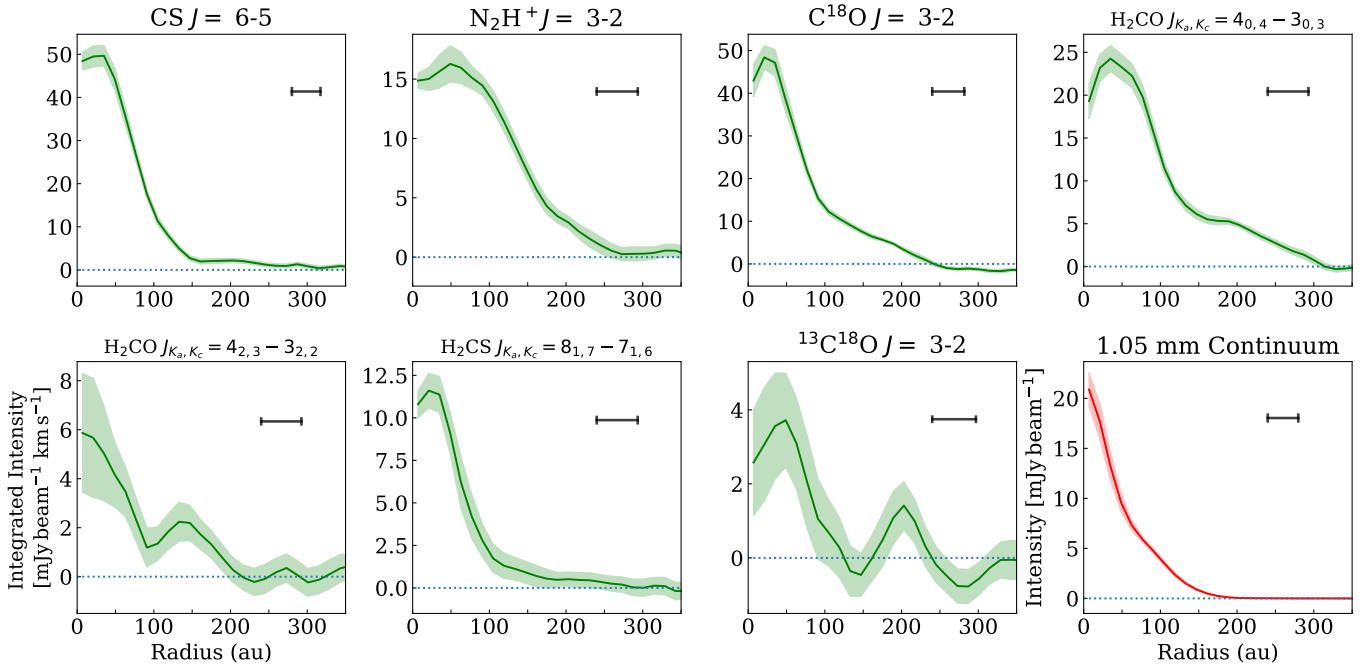


Figure 3. Deprojected, azimuthally-averaged radial profiles for each line and the 1.05 mm dust continuum. The shaded areas show the statistical 1σ uncertainty. The horizontal black lines show the scale of the synthesized beam.

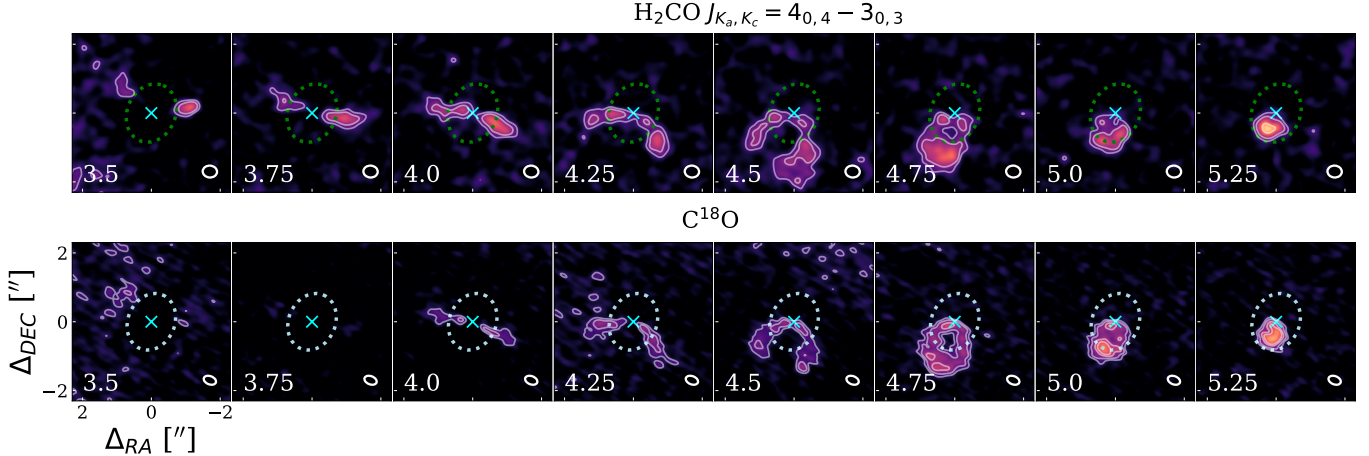


Figure 4. Subset of channels of H_2CO $4_{0,4} - 3_{0,3}$ and C^{18}O where an annular gap in emission is visible. Ellipses are drawn with the same P.A. and inclination as the GY 91 disk to denote the radius at which the break in emission is observed. The semi-major axis of the H_2CO ellipse is 122 au, while that for C^{18}O is 118 au. Contours correspond to 3, 5, 10, and 15σ , where σ is the rms listed in Table 3.

shifted (southeast) side ($4 \text{ km s}^{-1} < v_{lsrk} < 7 \text{ km s}^{-1}$) and calculating the radial profiles using an azimuthal mask over a particular position angle range. For H_2CO , we selected the region from $157 \pm 75^\circ$. For C^{18}O , we selected a slightly smaller region ($\pm 60^\circ$) due to the stronger cloud contamination.

The radial profiles of CS and H_2CS are similar, with both lines peaking at a radius of ~ 25 au and most of the emission originating from within ~ 150 au. The CS emission additionally shows a faint emission shelf out to ~ 300 au, which is not seen in H_2CS (Figure 3). This difference may be due to the higher S/N of the CS emission. N_2H^+ peaks further out at ~ 50 au and extends to ~ 250 au. While the radial profiles of C^{18}O and H_2CO $4_{0,4} - 3_{0,3}$ appear to have a central dip, this may be an artifact from having to exclude part of the disk from the radial profile calculation due to foreground absorption. H_2CO $4_{0,4} - 3_{0,3}$ shows a small decrement at ~ 150 au and bump at ~ 200 au, outside the millimeter continuum ($R_{90} = 117$ au; see Appendix C). The C^{18}O profile shows a tail over the same radial range where H_2CO has an emission bump. This substructure is also seen in some of the individual channels, where there appears to be an emission gap along the wings of the Keplerian pattern (Figure 4). We also see fluctuations in the radial profile of H_2CO $4_{2,3} - 3_{2,2}$ (Figure 3), but this is likely due to the low S/N.

3.2. Column Density Estimates

Fluxes for each line were calculated after applying a Keplerian mask to the image cubes to minimize contributions from cloud contamination. To calculate flux errors, we used the Keplerian mask to obtain 200 flux

samples of random regions off-source and then took the standard deviation. The fluxes are listed in Table 3.

Assuming that the line emission is optically thin and in local thermal equilibrium and that any background emission is small compared to the line emission, the disk-averaged column density can be estimated with the following formula (e.g., Goldsmith & Langer 1999; Bisschop et al. 2008):

$$N = \frac{4\pi S_\nu \Delta\nu Q(T)}{A_{ul} \Omega h c g_u} e^{E_u/T}, \quad (1)$$

where $S_\nu \Delta\nu$ is the integrated flux over the disk, $Q(T)$ is the partition function, A_{ul} is the Einstein coefficient, g_u is the upper state degeneracy, and Ω is the solid angle subtended by the region in which the emission is measured. For our flux measurements, Ω corresponds to the ellipse spanning the Keplerian mask used to extract the disk fluxes. To assess whether the optically thin approximation is reasonable, we checked the peak brightness temperatures (calculated using the full Planck equation) of each line from the image cubes. Most have peak brightness temperatures < 10 K, below the typical gas temperatures of $\sim 20 - 50$ K probed by ALMA molecular emission (e.g. Law et al. 2021). The peak brightness temperatures of C^{18}O (12 K) and CS (17 K) are colder than the expected gas temperatures, although not to as great a degree as the other targeted molecules. Therefore the optically thin approximation generally seems to be reasonable, although the CS column density may be somewhat underestimated depending on the actual temperature.

Based on the range of excitation temperatures estimated for the targeted molecules in other systems (e.g. Le Gal et al. 2019; Qi et al. 2019; Pegues et al. 2020;

Law et al. 2021), we calculate the column densities assuming gas temperatures of 20 and 50 K. The H₂CO and H₂CS column densities are calculated assuming a standard ortho-to-para ratio of 3 (although Guzmán et al. (2018) and Terwisscha van Scheltinga et al. (2021) found that the ortho-to-para ratio of H₂CO might be lower in the cold regions of disks). For H₂CO, we only use the para 4_{0,4} – 3_{0,3} transition to estimate the column density because the para 4_{2,3} – 3_{2,2} emission is only marginally detected in the image cube. While the weaker H₂CO line is well-detected with the matched filter method, and ratios of impulse responses for different transitions of the same species have been used as proxies for the flux ratios (e.g., Carney et al. 2017; Loomis et al. 2018), this kind of estimate could be problematic for our H₂CO observations given the strong cloud contamination. For CS, H₂CS, and N₂H⁺, the fluxes are taken from Table 3. Because the blueshifted side of the disk is heavily cloud-contaminated in C¹⁸O and H₂CO 4_{0,4} – 3_{0,3}, we estimated the total disk emission for these two lines by measuring the integrated flux redward of the systemic velocity and multiplying by 2, obtaining a value of 690 mJy km s⁻¹ for C¹⁸O and 430 mJy km s⁻¹ for H₂CO. A 10% systematic flux calibration uncertainty is assumed. The spectroscopic parameters and disk-averaged column densities for lines that are firmly detected in the images are listed in Table 4.

4. STELLAR HOST DYNAMICAL MASS ESTIMATE

To better understand the physical properties of the YSO and disk, it is essential to obtain an estimate of the stellar mass. We modeled the Keplerian rotation traced by CS to estimate the dynamical stellar mass (e.g., Simon et al. 2000; Rosenfeld et al. 2012). CS was chosen for this analysis because of its high S/N and minimal cloud contamination.

4.1. Image plane modeling

We used the `bettermoments` package (Teague & Foreman-Mackey 2018; Teague 2019b) to create a CS moment 1 map (masking pixels with S/N < 5) and estimate the associated uncertainties. The moment map was downsampled by the beam size so that adjacent pixels are independent. The moment map was then modelled with the `eddy` (Teague 2019c) package as a geometrically thin, Keplerian disk. The line-of-sight velocity is expressed as

$$v_0 = \sqrt{\frac{GM_*}{r}} \times \cos \phi \times \sin i + v_{\text{sys}} \quad (2)$$

where r is the radial separation from the star in the disk frame in units of arcseconds, ϕ is the polar angle in the disk frame, and v_{sys} is the systemic velocity.

Given the degeneracy between the mass of the central object (M_*) and the disk inclination (i), we fixed i to 36°.4 and the position angle (P.A.) to 157°.6 based on the parametric continuum modeling presented in Appendix C. The distance was also fixed to 140 pc. Thus, the model has four free parameters: the disk center offsets from the phase center Δx and Δy , M_* , and v_{sys} . We set the priors to the `eddy` default uniform priors. The package then uses Equation 2 to generate model moment 1 maps and samples the posteriors using the affine invariant Markov Chain Monte Carlo package `emcee` (Foreman-Mackey et al. 2013). We used 128 walkers over 2000 steps, with the first 1000 steps set aside as burn-in. The posterior medians and 68% confidence intervals are listed in Table 5. We present a full-resolution moment-1 map (i.e., without any downsampling), a model moment 1 map generated using the best-fit model values, and the residuals in Figure 5.

The best-fit model yields a dynamical stellar mass of $0.58 \pm 0.006 M_\odot$. As noted in Keppler et al. (2019), the formal uncertainties from `eddy` are very small and may be underestimated due to systematic error. To assess the robustness of our dynamical mass estimate, we compare our `eddy` results to those of the `DiskJockey` dynamical mass modeling code in the following section.

4.2. Visibility modeling

To obtain an independent estimate of the dynamical stellar mass, we also used the `DiskJockey` code (Czekala et al. 2015) to model the CS kinematics. Whereas `eddy` uses analytic expressions for the line-of-sight velocity to generate synthetic moment 1 maps to compare to the observed moment 1 maps, `DiskJockey` uses the RADMC3D radiative transfer code (Dullemond 2012) to generate line image cubes and then the corresponding visibilities to compare to observed visibilities. The advantages of `eddy` are that it is orders of magnitude less computationally intensive than `DiskJockey` and does not require parametrization of surface density or temperature profiles, which may be very complex for certain disks. The advantages of `DiskJockey` are that uncertainties are better quantified by fitting in the uv plane because the visibilities are independent and that it directly accounts for the effects of uv sampling (note, for instance, that `eddy` will generally have strong residuals at the disk center due to beam dilution, as seen in Figure 5).

The `DiskJockey` model setup is described in detail in Czekala et al. (2015). The disk is assumed to be geo-

Table 4. Disk-averaged column densities

Targeted Line	E_u (K)	Rest Frequency (GHz)	g_u	A_{ul} (s^{-1})	Q (20 K) (cm^{-2})	N (20 K) (cm^{-2})	Q (50 K) (cm^{-2})	N (50 K) (cm^{-2})
$H_2CS\ J_{K_a,K_c} = 8_{1,7} - 7_{1,6}$ (ortho)	73.4	278.8876613	51	3.18×10^{-4}	155	$(5.1 \pm 1.0) \times 10^{12}$	425	$(1.5 \pm 0.3) \times 10^{12}$
$N_2H^+\ J = 3 - 2$	26.8	279.5117491	63	1.26×10^{-3}	83.6	$(2.3 \pm 0.2) \times 10^{11}$	204.3	$(2.5 \pm 0.3) \times 10^{11}$
$H_2CO\ J_{K_a,K_c} = 40,4 - 30,3$ (para)	34.9	290.623405	9	6.90×10^{-4}	13.6	$(4.3 \pm 0.4) \times 10^{12}$	51.7	$(5.7 \pm 0.6) \times 10^{12}$
$CS\ J = 6 - 5$	49.4	293.9120865	13	5.23×10^{-4}	17.4	$(4.7 \pm 0.5) \times 10^{12}$	42.9	$(2.6 \pm 0.3) \times 10^{12}$
$C^{18}O\ J = 3 - 2$	31.6	329.33055250	7	2.17×10^{-6}	7.9	$(3.4 \pm 0.3) \times 10^{14}$	19.3	$(3.2 \pm 0.3) \times 10^{14}$

NOTE—Values for A_{ul} , E_u , g_u , and Q (interpolated) taken from Cologne Database for Molecular Spectroscopy (CDMS) (Endres et al. 2016). The H_2CO and H_2CS column density estimates correspond to an ortho-to-para ratio of 3:1.

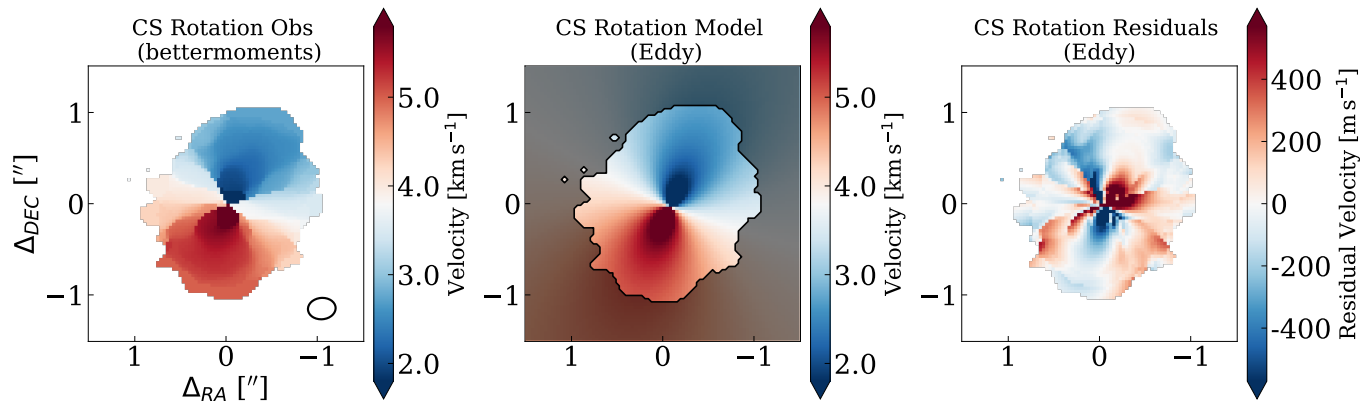


Figure 5. Left: CS moment 1 map generated from `bettermoments` without down-sampling. The synthesized beam is shown in the lower right corner. Middle: Model line-of-sight velocity map based on best-fit parameters from `eddy`. Right: Residuals from subtracting the model map in the center panel from the observed map in the left panel.

Table 5. eddy stellar dynamical mass model parameters

Parameter	Value
Δx (arcsec)	-0.0733 ± 0.003
Δy (arcsec)	-0.0322 ± 0.005
M_* (M_\odot)	0.5809 ± 0.006
v_{sys} (m/s)	3870.2 ± 6.9

metrically thin, axisymmetric, and in hydrostatic equilibrium. The temperature is modeled as a power-law,

$$T(r) = T_{10} \left(\frac{r}{10 \text{ au}} \right)^q, \quad (3)$$

where r is the radial distance from the star in cylindrical coordinates, and T_{10} and q are free parameters. Because the CS radial profile exhibits a slight dip in the center, we selected the Nuker profile (Lauer et al. 1995) option to model the gas surface density:

$$\Sigma_g(r) \propto \left(\frac{r}{r_T} \right)^{-\gamma} \left(1 + \left(\frac{r}{r_T} \right)^\alpha \right)^{\frac{\gamma-\beta}{\alpha}} \quad (4)$$

The Nuker profile breaks the disk into two regions, with r_T denoting the radius at which the transition between the two regions occurs and α controlling the sharpness of the transition (higher values have sharper transitions). The γ parameter determines the steepness of the profile in the inner region, with a negative value corresponding to a cavity. The β parameter determines the steepness of the profile in the outer region. Tripathi et al. (2017) illustrates how the Nuker profile varies with different choices of values. `DiskJockey` determines the normalization constant for the gas surface density profile based on the input for the total disk gas mass, M_{gas} . Additional free parameters include M_* , v_{sys} , the microturbulence level ξ (which contributes to line broadening), and the disk offsets from the phase center (Δx , Δy). We fixed the source distance to 140 pc. The P.A. and inclination were fixed to the values derived from modeling the high resolution continuum (Appendix C). Thus, our model has a total of 12 free parameters.

We assume that the CS:H₂ abundance is 10^{-8} , motivated by chemical models (Gross & Cleeves 2025). We note that in general, CS is not well-represented by a constant abundance. However, `DiskJockey` uses the CS abundance and total gas density to calculate the CS number densities, which are then fed into RADMC-3D for a local thermal equilibrium calculation. Thus, the gas surface density profile and the CS abundance are completely degenerate. For this reason, we emphasize that the M_{gas} estimate from `DiskJockey` should not be treated as a meaningful estimate of the disk mass.

Table 6. `DiskJockey` stellar dynamical mass model parameters

Parameter	Priors	Value
Δx (arcsec)	Uniform(-0.3 , 0.3)	-0.024 ± 0.001
Δy (arcsec)	Uniform(-0.3 , 0.3)	0.006 ± 0.001
M_* (M_\odot)	Uniform(0.1 , 2.0)	0.573 ± 0.002
v_{sys} (km s $^{-1}$)	Uniform(3.5 , 4.0)	3.858 ± 0.002
T_{10} (K)	Uniform(10 , 100)	$21.3_{-0.6}^{+1.0}$
q	Uniform(0 , 2)	$0.2_{-0.01}^{+0.03}$
Nuker r_T (au)	Uniform(10 , 200)	32 ± 3
Nuker γ	Uniform(-5 , 0)	$-3.0_{-1.1}^{+0.8}$
Nuker $\log \alpha$	Uniform(0 , 5)	$1.4_{-0.6}^{+0.8}$
Nuker β	Uniform(0 , 10)	$3.91_{-0.06}^{+0.05}$
ξ (km s $^{-1}$)	Uniform(0 , 0.5)	0.199 ± 0.005
$\log M_{\text{gas}}/M_\odot$	Uniform(-4 , -0.1)	$-3.67_{-0.07}^{+0.06}$

`DiskJockey` uses a Julia implementation of the `emcee` code to sample the posterior distributions. Uniform priors (listed in Table 6) were chosen based on visual inspection of the CS data as well as `DiskJockey` model results for other disks (Czekala et al. 2015, 2017). We used 48 walkers over 9000 steps, including a burn-in period of 3000 steps. Following Czekala et al. (2017), we assessed convergence by checking that the Gelman-Rubin statistic \hat{R} (Gelman et al. 2014) was < 1.1 for each parameter. The exception was $\log \alpha$, which had a slightly higher value of 1.2. The values for $\log \alpha$ are not well-constrained because of the moderate angular resolution of our observations, which cannot rule out the possibility of very sharp transitions in the Nuker profile. However, this is not important for replicating the kinematic pattern of the CS emission. Table 6 reports the medians of the posterior distributions as well as the uncertainties calculated from the 16th and 84th percentiles. A comparison of the channel maps of the observations, best-fit model, and residuals are shown in Figure 6. Some moderate residuals are visible in the southeast of the disk at velocities of $\sim 5.25 - 5.5$ km s $^{-1}$ due to the slight asymmetry of the CS emission, but the model otherwise appears to reproduce the data well. The derived M_* value of $0.573 M_*$ agrees well with the `eddy` value, within two percent.

We also note that while the distances were fixed in the models, the stellar mass scales linearly with distance, so what we have estimated in practice is $M_* \left(\frac{d}{140 \text{ pc}} \right)$. Cánovas et al. (2019) find that the dispersion of the YSOs in Ophiuchus with *Gaia* parallaxes is ~ 8 pc. Since the distance we use for GY 91 is based on the median value for the region, this implies an uncertainty on the distance of GY 91 of $\sim 6\%$.

5. GAUGING ENVELOPE CONTRIBUTIONS TO OBSERVED EMISSION

5.1. *Dust continuum emission*

Federman et al. (2023) suggested using the ratio of the 870 μm 12-m and ACA continuum fluxes to probe the contributions of the envelope to the overall dust emission in YSOs. Due to its shorter baselines, the ACA is more sensitive to large-scale emission from envelopes, while 12-m observations resolve out more of the envelope emission and are often dominated by the smaller-scale disk emission. Federman et al. (2023) defined a ratio of $R < 0.5$ as envelope-dominated and $R > 0.5$ as disk-dominated emission, where R is the ratio of the 12-m to ACA fluxes.

Our closest observed continuum wavelength to the Federman et al. (2023) observations is at 930 μm . We split out our 930 μm ACA observations and the extended 12-m array configuration observations (corresponding to the observations dated 2022 June 10 and 11 with baselines of 15-1200 m in Table 1) from our final self-calibrated continuum measurement set and imaged the ACA and 12-m observations separately. The MRS is ~ 3000 au for the ACA-only observations and ~ 530 au for the extended 12-m observations. As in Federman et al. (2023), we estimated the total flux in each image by calculating the flux within ellipses of increasing sizes until the flux measurements leveled out. The flux in the image produced from the extended 12-m array observation is 221 mJy, while the flux measured from the ACA observations is 218 mJy. This yields $R \sim 1$, suggesting that the emission is disk-dominated. While the ACA flux measurement is slightly lower, which may seem counterintuitive, the difference is only $\sim 1\%$, which is in line with the small percentage variations between observations in different configurations that were noted in the exoALMA survey of Class II disks (Loomis et al. 2025).

5.2. *Molecular line emission*

We explored whether any of the large-scale emission observed in C^{18}O and H_2CO might originate from an envelope component, as opposed to a foreground cloud, by comparing observed moment 1 maps to synthetic moment 1 maps. We used the Flat Envelope Model with Rotation and Infall under Angular Momentum Conservation (FERIA) package (Oya et al. 2022) to generate a synthetic image cube of a Keplerian disk with a ballistic infalling-rotating envelope. Based on eddy modeling of the Keplerian disk in CS emission (Section 4), we set the protostellar mass to $0.58 M_\odot$, the systemic velocity to 3.87 km s^{-1} , the disk inclination to $36^\circ.4$, and the P.A. to $157^\circ.6$. The radius of the centrifugal barrier was set

to 300 au (approximately the extent of the emission detected from the Keplerian disk) and the envelope radius was set to 600 au (chosen to be large enough to visualize the envelope kinematics clearly). We adopted a flaring angle of 30° and a density profile of $n(r) \propto r^{-1.5}$. The temperature profile is assumed to follow $T(r) \propto r^{-0.5}$ within the disk and is set to a value of 10 K at the envelope-disk boundary and throughout the envelope. We note, however, that the parameters that mainly control the appearance of the synthetic moment 1 map are the protostellar mass, orientation of the system, and the centrifugal and envelope radii. FERIA calculates relative intensities assuming optically thin emission, with the absolute intensity scale being arbitrary. The resulting image cube was convolved to the same angular resolution as the GY 91 observations.

The moment 1 map generated from the FERIA model is shown in Figure 7, along with moment 1 maps of H_2CO $4_{0,4} - 3_{0,3}$ and C^{18}O generated from images with a $0''.2$ *uv* taper applied in order to increase sensitivity to the larger-scale emission. The kinematics of the emission outside of the disk do not appear to match that of the infalling-rotating envelope in the FERIA model. We only observe large-scale emission at blueshifted velocities surrounding the disk, while the FERIA model predicts both redshifted and blueshifted envelope emission. As such, the observed large-scale emission does not exhibit clear envelope signatures. That said, infalling material in Class 0 and I systems often exhibit more complex morphologies than the axisymmetric model adopted by FERIA. Extended infalling streamers feeding material to disks from the cloud have been detected in YSOs ranging from Class 0 to Class II (e.g., Ginski et al. 2021; Valdivia-Mena et al. 2022; Pineda et al. 2023; Taniguchi et al. 2024; Tanius et al. 2024). However, the extended emission observed in H_2CO and C^{18}O does not exhibit the narrow and elongated morphologies commonly associated with streamers. Using single-dish CO maps, de Geus et al. (1990) measured a systemic velocity of 3.03 km s^{-1} for the ρ Oph cloud complex containing GY 91, which is consistent with the dominant velocities of the large-scale H_2CO and C^{18}O emission that we observe. The large-scale emission around GY 91 therefore appears likely to be associated with foreground cloud material.

6. DISK MASS ESTIMATES

6.1. *Radiative transfer modeling of dust continuum*

We used the Monte Carlo radiative transfer code MCFOST (Pinte et al. 2006, 2009) to model our 0.93 and 1.05 mm dust continuum observations. While our observations are at lower angular resolution than those of

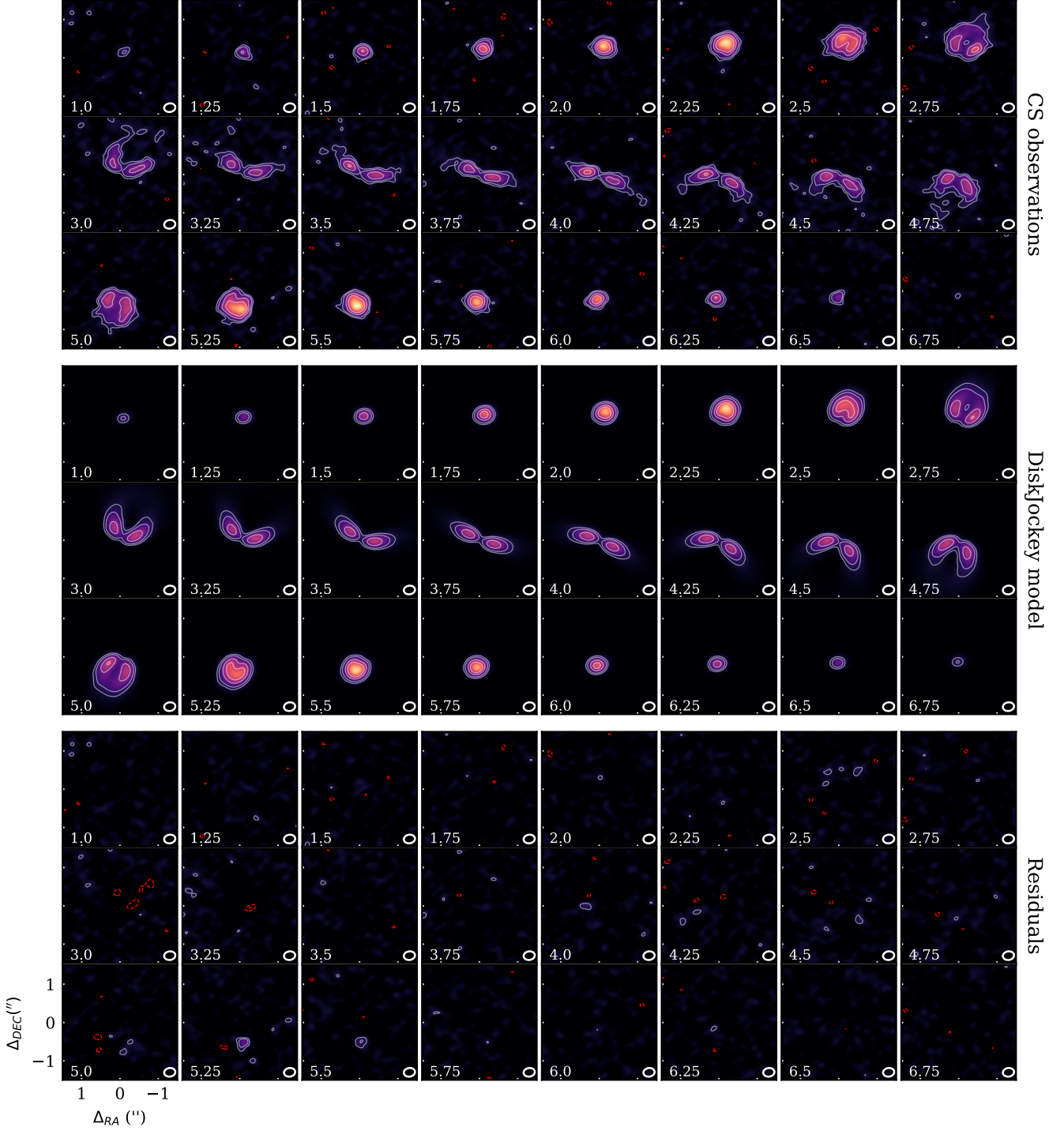


Figure 6. A comparison of channel maps of the CS observations, best-fit DiskJockey model, and residuals, all on the same color scale. The white solid contours correspond to the $[3, 5, 10, 15]\sigma$ levels and the red dashed contours correspond to the -3σ level, where σ is the rms listed in Table 3. The synthesized beam is plotted in the lower right corner of each panel, while the LSRK velocity is in the lower left corner.

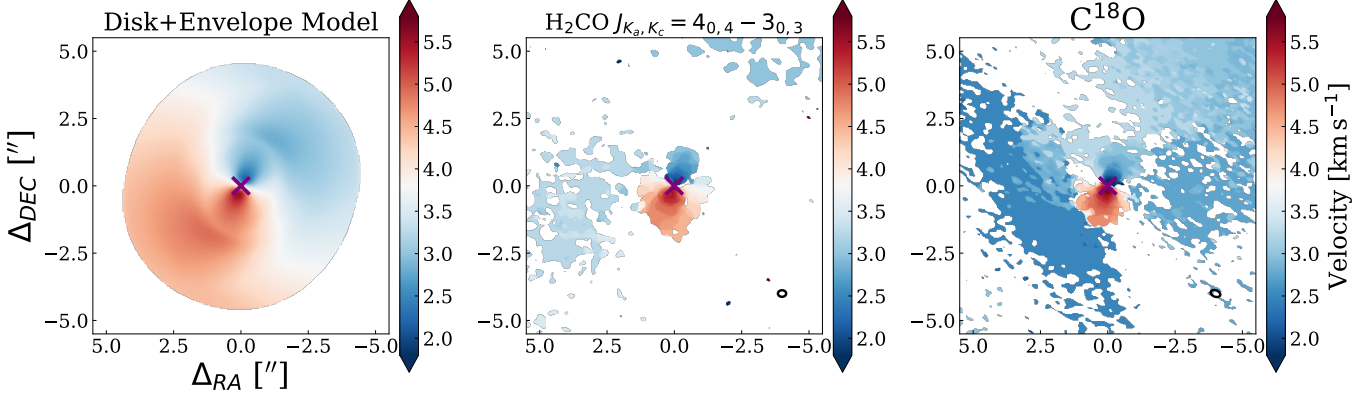


Figure 7. Left: FERIA model moment 1 map of disk and infalling envelope. Middle: Tapered ($0.2''$) moment 1 map of H_2CO $J_{K_a, K_c} = 4_{0,4} - 3_{0,3}$. Right: Tapered ($0.2''$) moment 1 map of C^{18}O . The field of view is expanded compared to Figure 2 in order to show the large-scale non-disk emission better. The synthesized beam is shown in the lower right corner.

Sheehan & Eisner (2018) and Cieza et al. (2021), our observations have better uv coverage at short baselines, which yields better sensitivity at larger scales and more accurate fluxes. We elected not to attempt to fit the SED simultaneously, given that the heavy cloud contamination would likely have a significant influence on the infrared emission, as previously noted by McClure et al. (2010).

We adopt MCFOST’s power-law disk model option. The disk surface density as a function of radius r in cylindrical coordinates is parametrized as:

$$\Sigma(r) \propto r^p \quad (5)$$

where p is the surface density exponent. Given an input disk mass, MCFOST computes a normalization factor for the surface density. The inner radius of the disk (R_{in}) was fixed to 0.1 au, while the outer radius R_{out} is left as a free parameter.

The disk scale height is parametrized as

$$h(r) = h_0 \left(\frac{r}{R_{\text{ref}}} \right)^\beta, \quad (6)$$

where h_0 is the disk scale height in au at the reference radius R_{ref} , and β is the flaring exponent. Since our millimeter continuum observations do not constrain the disk vertical structure, we fixed h_0 to 10 au, R_{ref} to 100 au, and β to 1.2, motivated by values that have previously been inferred from radiative transfer modeling of protoplanetary disks (e.g., Zhang et al. 2021).

Dust grain sizes were assumed to have a power-law distribution $n(a) \propto a^{-3.5}$, following Mathis et al. (1977). Grain sizes ranged from 0.01 to 1000 μm . We adopted the DSHARP dust composition (Birnstiel et al. 2018) and used the `dsharp_opac` package (Birnstiel et al. 2018) to retrieve the wavelength-dependent optical constants,

which originated from Henning & Stognienko (1996); Draine (2003); Warren & Brandt (2008).

Doppmann et al. (2005) measured an effective temperature of 3300 K for GY 91 and a stellar luminosity of $L_* = 1.7 L_\odot$. Approximating the star as a perfect blackbody ($L_* = 4\pi R_*^2 \sigma_{\text{SB}} T_{\text{eff}}^4$), we derive a stellar radius of $3.99 R_\odot$. These values of T_{eff} and R_* are used as inputs for MCFOST.

Using the values obtained from parametric modeling of the dust continuum (Appendix C), the P.A. was set to $157^\circ.6$ and the inclination to $36^\circ.4$. We generated different models by varying the dust disk mass (M_{dust}), the surface density exponent p , and the outer radius R_{out} . We then convolved the synthetic continuum image produced by MCFOST with a 2D Gaussian with the same dimensions as the synthesized beam to compare to the observations. We found that $M_{\text{dust}} = 44 M_\oplus$, $p = -0.4$, and $R_{\text{out}} = 140$ au provided a good visual match to the continuum radial profiles. The parameters of our best model are presented in Table 7. We also examined the range of dust masses that would be consistent with the radial profile, given the 10% systematic flux calibration uncertainty, and found that masses of roughly $39\text{--}49 M_\oplus$ were compatible. Figure 8 shows a comparison between the model and the observed continuum radial profiles at 0.93 and 1.05 mm. Assuming an ISM-like gas-to-dust ratio of 100, a dust mass of $44 M_\oplus$ corresponds to a total disk mass of $0.013 M_\odot$ ($4400 M_\oplus$).

6.2. Disk mass estimate from N_2H^+ and C^{18}O

The combination of N_2H^+ and C^{18}O is useful for inferring disk masses because N_2H^+ helps to break the degeneracy between the CO:H₂ ratio and the total gas mass (e.g., Anderson et al. 2019; Trapman et al. 2022). We used the method presented in Trapman et al. (2025a,b) to estimate the disk gas mass of GY 91 based on its N_2H^+ and C^{18}O integrated fluxes (as well as the 1.05

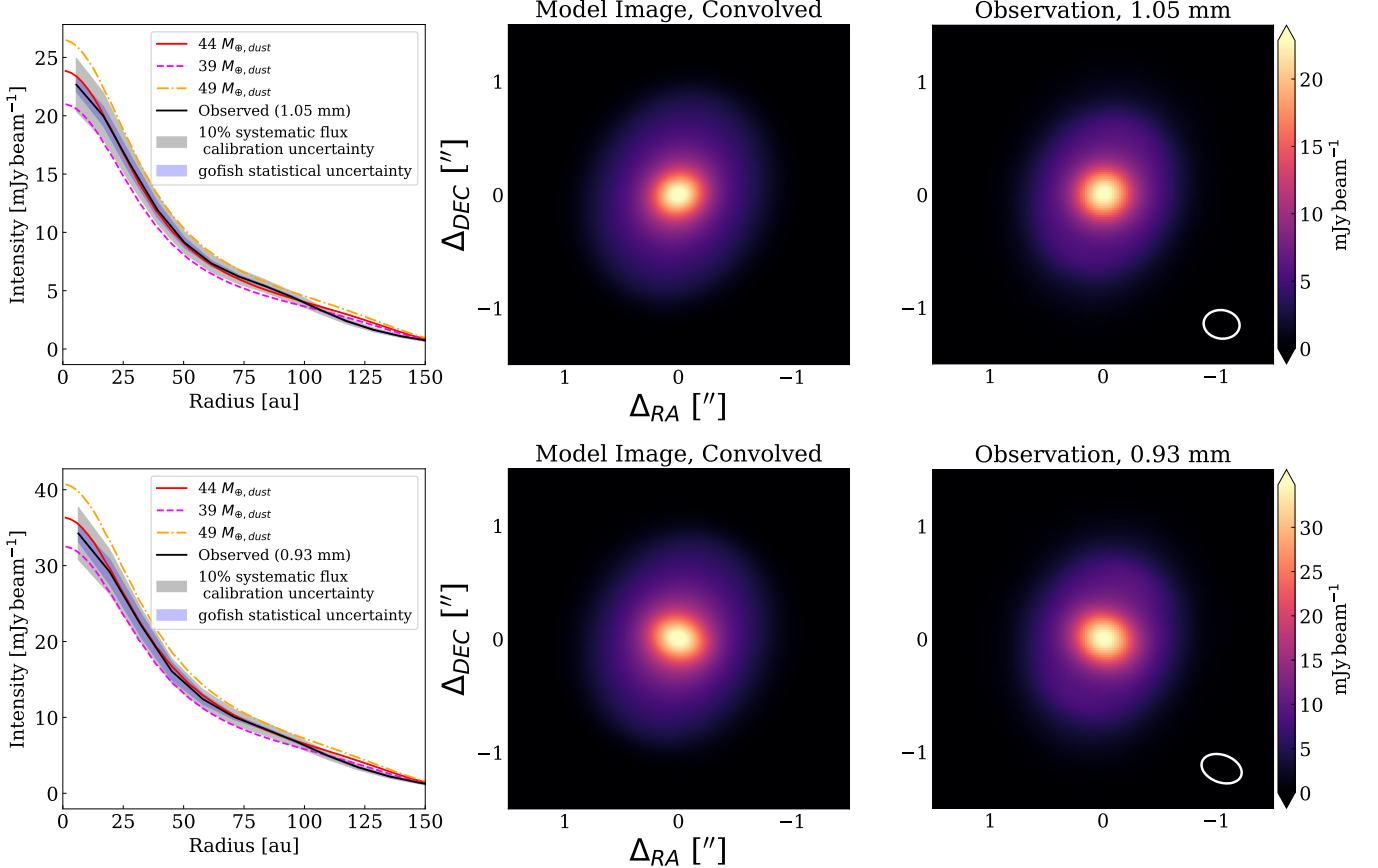


Figure 8. Left panels: Comparison between the radial profiles of the 1.05 (top)/0.93 (bottom) mm dust continuum observations. The blue shaded region indicates the uncertainty computed with `gofish` based on the scatter of the data and the gray shaded region shows the 10% flux calibration uncertainty. Different linestyles correspond to models with different masses. Middle panels: Model image of 44 M_{\oplus} disk from MCFOST convolved with the observed beam. Right panels: Observed dust continuum image (1.05 mm on top, 0.93 mm on bottom) with the beam size indicated on the bottom right corner of each panel.

Table 7. MCFOST best-fit dust continuum model parameters

Parameter	Value ^a
h_0 (au)	10
R_{in} (au)	0.1
R_{out} (au)	140
R_{ref} (au)	100
Surface density exponent p	-0.4
Flaring exponent β	1.2
M_{dust} (M_{\oplus})	44

^aValues for p , M_{dust} , and R_{out} were varied, while other parameter values were held fixed.

mm continuum to estimate the gas-to-dust ratio). Trapman et al. (2025a,b) used the DALI thermochemical code (Bruderer et al. 2012; Bruderer 2013) to generate a grid of disk models with different values for the disk gas mass (M_{gas}), characteristic radius (R_c), stellar lu-

minosity, disk flaring parameter (ψ), gas-to-dust ratio, fraction of dust mass in large grains, midplane cosmic ray ionization rate (ζ_{mid}), and fractional CO abundance (x_{CO}). They performed raytracing at different disk inclinations to generate line and continuum flux and emission size estimates for each model. They then generated a more finely sampled grid through interpolation. Posterior distributions for M_{gas} , R_c , the gas-to-dust ratio, x_{CO} , and ζ_{mid} can be sampled using `emcee` (Foreman-Mackey et al. 2013) by comparing the model fluxes and convolved emission sizes to the available observed fluxes and sizes. In this modeling framework, the posterior of L_* is also sampled, but because the chemical models do not place strong constraints on L_* , its posterior distribution is essentially set by the choice of the prior.

The N₂H⁺ and 1.05 mm continuum fluxes were taken from Table 3. For C¹⁸O, we used the same flux value as that used for calculating column densities in Section 3 (i.e., multiplying the flux from the redshifted side by two due to the cloud contamination on the blueshifted

Table 8. Gas mass modeling results

Parameter	Value ^a
M_{gas} (M_{\odot})	$0.008^{+0.04}_{-0.005}$
$\log(\text{gas-to-dust ratio})$	$1.7^{+0.3}_{-0.2}$
$\log x_{\text{CO}}$	-4.6 ± 0.3
R_c (au)	80 ± 40
$\log(\zeta_{\text{mid}}/\text{s}^{-1})$	$-17.9^{+0.6}_{-0.8}$

^aValues correspond to posterior medians, while uncertainties are computed from the 16th and 84th percentiles

side). A 10% systematic flux calibration uncertainty was assumed for the continuum and N_2H^+ , while we adopted a larger uncertainty of 20% for C^{18}O given the need to approximate the total flux by using the non-contaminated side of the disk. We used the C^{18}O radial profile (Figure 3) to estimate R_{90} , the disk radius that encloses 90% of the C^{18}O flux, and obtained a value of 185 au. Again, given the impact of cloud contamination, we conservatively estimate an uncertainty of ± 40 au on the R_{90} value, corresponding to roughly $2\times$ the standard deviation of the synthesized beam. Based on the L_* measurement from Doppmann et al. (2005), we adopted a Gaussian prior for L_* centered at $1.7 L_{\odot}$ with a standard deviation of $0.5 L_{\odot}$ (corresponding to $0.3L_*$). Following Trapman et al. (2025a), we set flat priors with bounds of $[-4, -0.3]$ for $\log M_{\text{gas}}/M_{\odot}$, $[1, 3]$ for the log of the gas-to-dust ratio, $[-6.5, -4]$ for $\log x_{\text{CO}}$, $[15, 200]$ au for R_c , and $[-19, -17]$ for $\log(\zeta_{\text{mid}}/\text{s}^{-1})$.

We ran `emcee` with 128 walkers and 20,000 steps, including a burn-in of 5000 steps. The posterior medians and errors measured from the 16th and 84th percentiles are listed in Table 8. The median value for the gas mass ($0.008 M_{\odot}$) agrees within a factor of 2 of the disk mass estimate from the MCFOST model of the dust continuum. The uncertainties, though, from the N_2H^+ and C^{18}O modeling are very large. The uncertainties might be reduced either by observing the N_2H^+ 4 – 3 transition or C^{17}O , which were also computed in the Trapman et al. (2025a) model grids. ($^{13}\text{C}^{18}\text{O}$ was not included in their grids).

The Trapman et al. (2025a,b) models were designed for Class II disks, so envelopes were not incorporated into the source structures. Not accounting for envelope backwarming could lead to underestimates in disk temperatures (e.g., Butner et al. 1994; D’Alessio et al. 1997), which in turn would lead to overestimates in disk masses. To assess whether GY 91’s behavior differs substantially from Class II disks, we compare its C^{18}O and N_2H^+ fluxes to those of Class II disks hosted by K and M stars in Figure 9. The sources chosen for comparison are the

disks with N_2H^+ and C^{18}O detections that were compiled and modelled by Trapman et al. (2025a,b). (We exclude the disks hosted by earlier type stars because Trapman et al. (2025a) show that they have higher C^{18}O fluxes compared to K and M stars with similar N_2H^+ fluxes.) Generally speaking, the C^{18}O and N_2H^+ fluxes for disks hosted by K and M stars tend to increase together, with a possible flattening-out of the C^{18}O fluxes at the upper end of the N_2H^+ fluxes. GY 91 appears to fall in a similar part of the C^{18}O vs. N_2H^+ flux plot as the Class II disks hosted by K and M stars. It is also interesting to compare GY 91’s fluxes to that of Elias 27. Elias 27 is commonly identified as a Class II disk, but its molecular emission shows that it is still partially embedded (Huang et al. 2018; Paneque-Carreño et al. 2021). Trapman et al. (2025a) pointed out that Elias 27 exhibits an elevated C^{18}O flux compared to other Class II disks with similar N_2H^+ fluxes. They suggested that envelope backwarming could lead to less CO depletion compared to the other Class II disks. If this is the case, then GY 91 does not appear to show a similar influence from an envelope.

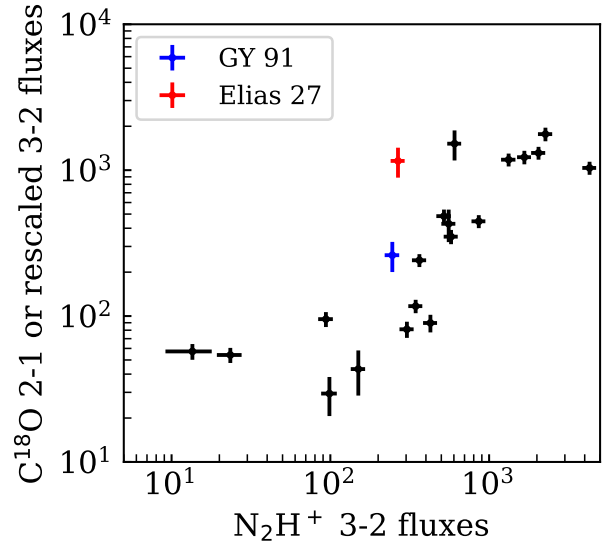


Figure 9. A comparison of GY 91’s N_2H^+ and C^{18}O fluxes to a sample of Class II disks from Trapman et al. (2025a), scaled to a common distance of 150 pc. Following Trapman et al. (2025a), sources that only have C^{18}O 3-2 fluxes (including GY 91) are plotted with C^{18}O fluxes scaled down by a factor of 2.3 based on the 3 – 2/2 – 1 flux ratios calculated from their model grid. The 1σ error bars include the statistical uncertainty and an assumed 10% systematic flux calibration uncertainty.

7. DISCUSSION

7.1. Comparison with previous stellar and disk mass estimates for GY 91

Based on a T_{eff} estimate of 3300 K from Doppmann et al. (2005) and an estimated age of 0.5 Myr, Sheehan & Eisner (2018) derived a stellar mass of $0.25 M_{\odot}$ from the Baraffe et al. (2015) stellar evolutionary models. Our stellar dynamical mass measurement of $0.58 M_{\odot}$ is more than twice as large as the estimate. In a study of pre-main sequence stars with spectral types similar to GY 91 (i.e., around M4), Pegues et al. (2021) found that the masses derived from stellar evolutionary models could be up to 80% less than the dynamical mass estimate. Some of the explanations they proposed for the discrepancy were that the T_{eff} values were underestimated, that the sources could be unresolved binaries, or that a significant fraction of the stars are covered by starspots. One of these proposed explanations could also account for the discrepancy in the estimated stellar masses for GY 91.

Assuming optically thin emission and a uniform disk temperature of 20 K, Cieza et al. (2021) used the Hildebrand (1983) formula to convert millimeter continuum disk fluxes to dust masses and estimated a dust mass of $56 M_{\oplus}$ for GY 91. This corresponds to a total disk mass of $0.017 M_{\odot}$ for a gas-to-dust ratio of 100. Their estimate is comparable to our estimate from dust continuum radiative transfer modeling and about a factor of two larger than our disk mass estimate from N_2H^+ and C^{18}O .

On the other hand, Sheehan & Eisner (2018) reported a disk mass of $0.17 M_{\odot}$ from radiative transfer modeling, which is an order of magnitude larger than our disk mass estimate. Whereas we fixed L_* to $1.7 L_{\odot}$ and a_{max} to 1 mm, Sheehan & Eisner (2018) allowed these parameters to vary freely. Their best-fit model had $L_* = 0.11 L_{\odot}$ and $a_{\text{max}} = 83$ mm. Lower stellar luminosities would tend to drive disk mass estimates upward due to the lower temperature, while higher values of a_{max} would drive disk mass estimates upward due to the low opacities of large dust grains.

Doppmann et al. (2005) cautioned that their estimate of $L_* = 1.7 L_{\odot}$ is uncertain due to their extinction correction. Assuming no rotation and solar metallicity, the MIST stellar evolutionary models (Paxton et al. 2011; Choi et al. 2016; Dotter 2016) predict a stellar luminosity of $1.5 L_{\odot}$ for a $0.6 M_{\odot}$ star at an age of 0.5 Myr, which is similar to the estimated L_* from Doppmann et al. (2005). If we assume an older age of 1 Myr, the stellar luminosity drops to $0.8 L_{\odot}$. If the thermal structure is primarily set by stellar irradiation, then the disk

temperature scales as $T \propto L_*^{0.25}$ (e.g. Chiang & Goldreich 1997; D'Alessio et al. 1998). Thus, a factor of two uncertainty in the stellar luminosity should not lead to significant underestimates of the disk mass.

Spatially resolved multi-frequency studies of HL Tau, a Class I/flat spectrum disk with millimeter continuum gaps and rings, suggest that its a_{max} values range from 1 cm in the inner disk to $300 \mu\text{m}$ in the outer disk (e.g., Guerra-Alvarado et al. 2024). Therefore, the assumption of a single value of a_{max} in our work and in Sheehan & Eisner (2018) may be simplistic. Obtaining high-resolution, multi-band observations can enable the dust surface density, temperature, and a_{max} to be derived simultaneously as a function of disk radius (e.g., Macías et al. 2021).

In a comparison of gas mass estimates from C^{18}O and N_2H^+ fluxes to disk mass estimates from kinematic modeling, Trapman et al. (2025a) found that the latter tended to be larger than the former by a factor of ~ 2 . Thus, it is plausible that our disk mass for GY 91 is underestimated by a factor of a few. Given that we do not observe evidence of gravitational instability-induced spiral substructures (Goldreich & Lynden-Bell 1965), we use considerations of gravitational stability to estimate an upper bound on the disk mass. Protoplanetary disks are expected to become unstable at a disk-to-stellar mass ratio of $M_{\text{disk}}/M_* \gtrsim 0.1$ (e.g., Kratter & Lodato 2016). Given a stellar mass of $0.6 M_{\odot}$ for GY 91, we thus expect that the disk mass should not be substantially greater than $\sim 0.06 M_{\odot}$. This limit is lower than the Sheehan & Eisner (2018) disk mass estimate of $0.17 M_{\odot}$.

7.2. Comparison with other disks

As in previous ALMA observations of CS in Class I and II disks (e.g., Le Gal et al. 2019, 2021; Garufi et al. 2021; Huang et al. 2024), our CS radial profile shows a central dip, and the moment 0 maps show azimuthally asymmetric disk emission. In a survey of Class I/flat spectrum disks, Garufi et al. (2021) detected envelope emission in CS 5–4 in all sources. It is not clear whether the absence of obvious envelope emission in our CS 6–5 observations of GY 91 is due to less envelope material, or because we observed a transition with a higher E_u .

For GY 91, the redshifted side (southeast) is slightly brighter than the blueshifted side (northwest) of the disk in CS emission (Figure 1). While C^{18}O and H_2CO $4_{0,4} - 3_{0,3}$ show strong cloud contamination on their northwest sides that leads to the disk emission being absorbed, cloud contamination in CS is minimal. Furthermore, H_2CS exhibits a similar emission asymmetry as CS and shows no cloud contamination (Figure 1).

Azimuthal variations in surface density, temperature, or dust optical depth can contribute to CS asymmetries (e.g. [van der Plas et al. 2014](#)). The dust emission of GY 91 appears to be axisymmetric, making azimuthal surface density variations a less likely reason for the CS asymmetry. However, one cannot yet rule out possible azimuthal temperature variations due to shadowing from a misaligned inner disk, such as in HD 100546 ([Keyte et al. 2023](#)). [Le Gal et al. \(2021\)](#) speculated that CS asymmetries could arise due to disk jets or winds, but we do not see evidence of jets or winds within our observations or previous observations of GY 91. Chemical asymmetries may also arise due to heating from a protoplanet (e.g., [Cleeves et al. 2015](#)). Observations of other molecular lines or chemical modeling may shed light on the origins of the asymmetry in the sulfur-bearing lines.

[Garufi et al. \(2021\)](#) found that disk-averaged CS column densities in Class I/flat spectrum disks were typically an order of magnitude above that of Class II disks, although the number of measurements in each comparison group was only five and seven, respectively. Our disk-averaged CS column density estimate is similar to that of Class II disks ([Le Gal et al. 2019](#)). In addition, we estimate a disk-averaged H₂CS/CS column density ratio of $\sim 0.6 - 1.1$ (depending on the adopted excitation temperature), which is in line with values previously found for Class I and II disks (e.g. [Le Gal et al. 2019; Garufi et al. 2021; Le Gal et al. 2021](#)). [Le Gal et al. \(2021\)](#) interpreted such high H₂CS/CS ratios as evidence that organosulfur compounds contain a significant fraction of the sulfur reservoir.

The C¹⁸O and H₂CO 4_{0,4}-3_{0,3} moment 0 maps share similar morphologies, with a strong tail of emission beyond radii of 150 au. This may be a reflection of CO hydrogenation being one of the key pathways to forming H₂CO (e.g., [Hiraoka et al. 1994](#)), especially in the cold outer disk (e.g., [Pegues et al. 2020](#)). We also see a bump in the H₂CO radial profile at $r \sim 200$ au and hints of a gap at 120 au in the channel maps. These H₂CO features are further out than any substructures in the high-resolution dust continuum ([Cieza et al. 2021](#)) (see also [Appendix C](#)). Gaps in H₂CO beyond the dust continuum have commonly been reported in Class II disks ([Pegues et al. 2020; Guzmán et al. 2021; Facchini et al. 2021](#)). The H₂CO substructure may either reflect radial variations in the gas surface density (possibly associated with planet-disk interactions) or radial chemical variations. In the latter case, H₂CO substructure has been hypothesized to be due to changes in the relative importance of gas-phase and grain-surface pathways with disk

radius (e.g., [Loomis et al. 2015](#)) or to photodesorption outside the dust continuum (e.g., [Carney et al. 2017](#)).

[Garufi et al. \(2021\)](#) noted a possible dichotomy in the behavior of the disk-averaged CS/H₂CO column density ratios in Class I/flat spectrum disks versus Class II disks. The former tend to have ratios below unity ($\sim 0.2 - 0.6$), while the latter tend to have ratios of $\sim 2 - 3$. Our values for GY 91 lie somewhere in-between, ranging from 0.5 – 1.1 depending on the assumed excitation temperature. The [Garufi et al. \(2021\)](#) comparison was based on a small number of sources and heterogeneous observations, so a larger, uniform sample will be needed to assess the extent to which the CS/H₂CO column density ratio can be used as an evolutionary marker. We speculate that this trend could be linked to gas-phase C/O ratios increasing in the colder and more settled Class II disks (e.g., [Calahan et al. 2023](#)), but chemical modeling will be required to explore the factors affecting the CS/H₂CO ratio.

N₂H⁺ in GY 91 has a ring-like emission pattern, as is commonly observed in protoplanetary disks (e.g., [Qi et al. 2019; Trapman et al. 2025a](#)). The peak of the N₂H⁺ ring has been suggested to occur close to the CO snowline because N₂H⁺ is destroyed by CO (e.g., [Qi et al. 2013](#)). To examine whether that might be the case for GY 91, we plot the 2D temperature structure from our best-fit MCFOST dust continuum model ([Section 6](#)) along with 25 and 20 K contours in [Figure 10](#). Based on this temperature structure, the midplane CO snowline is expected to fall somewhere between 40 and 75 au. The peak of the N₂H⁺ radial profile ([Figure 3](#)) occurs at ~ 50 au, which is compatible with the expected snowline location based on radiative transfer modeling. However, other works have shown that the relationship between the N₂H⁺ distribution and the CO snowline is not necessarily straightforward ([van't Hoff et al. 2017; Qi et al. 2019](#)). [Qi et al. \(2019\)](#) noted that N₂H⁺ ring morphologies tend to fall into two categories: 1) Well-defined rings with narrow radial extents, combined with a faint, diffuse outer component and 2) broad rings. They suggested that these different morphologies were a consequence of temperature structures that are nearly vertically isothermal in the N₂H⁺ emitting region in the first case and temperature structures with a steep vertical gradient in the second case. The former types of rings are expected to be more reliable tracers of the CO snowline than the latter. The broadness of GY 91's N₂H⁺ ring could likewise point to a steep vertical temperature gradient, making it harder to reliably probe the midplane CO snowline location.

We also estimated the dust continuum spectral indices ($\alpha = \frac{\ln(I_{\nu_1}/I_{\nu_2})}{\ln(\nu_1/\nu_2)}$) using our observations at 0.93

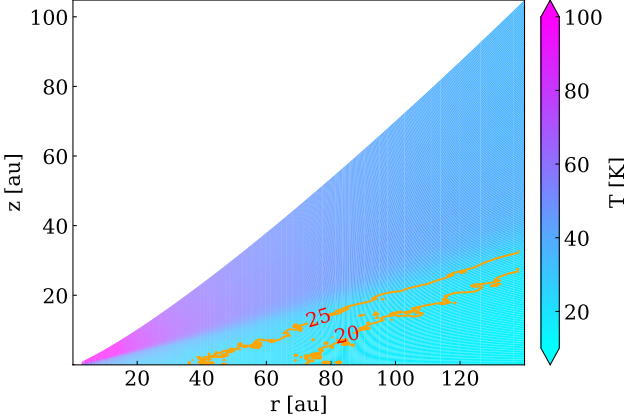


Figure 10. 2D temperature structure from our best MC-FOST radiative transfer model of the dust continuum. Contours correspond to 20 and 25 K in order to indicate the approximate range of locations of the CO snowline.

and 1.05 (Table 3) as well as the measurement of 97.5 mJy at 1.3 mm from Cieza et al. (2019). (These correspond to frequencies of 322, 286, and 225 GHz, respectively). A 10% systematic flux calibration uncertainty is assumed for each measurement. We find that $\alpha_{0.93 \text{ mm}-1.3 \text{ mm}} = 2.3 \pm 0.4$, $\alpha_{1.05 \text{ mm}-1.3 \text{ mm}} = 1.9 \pm 0.6$, and $\alpha_{0.93 \text{ mm}-1.05 \text{ mm}} = 3.0 \pm 1.1$. The measurement between 0.93 mm and 1.3 mm has the largest wavelength difference and therefore provides the best lever arm for estimating the spectral index. The spectral index is consistent with values measured for both young embedded disks (Cacciapuoti et al. 2025) and older Class II disks (Ricci et al. 2010), with some combination of optically thick emission and grain growth playing a role in setting these values.

7.3. What is the evolutionary status of GY 91?

As noted in the introduction, the evolutionary status of GY 91 has been debated due to the difficulty in disentangling the effects of envelope and foreground cloud. In Section 5, we estimated the $930 \mu\text{m}$ 12-m/ACA flux ratio, finding a value of ~ 1 . Federman et al. (2023) surveyed the $870 \mu\text{m}$ 12-m/ACA flux ratios for Class 0, I, and flat spectrum disks in Orion. They find that the ratio generally increases from Class 0 to flat spectrum sources and therefore suggested that the ratio could be used as an evolutionary marker. They find that $\sim 50\%$ of Class I disks have ratios < 0.6 and $\sim 70\%$ have ratios < 1 . This suggests that GY 91 is less embedded, and therefore perhaps more evolved, than the typical Class I YSO. In this case, GY 91 may not be an example of particularly early formation of disk substructures.

One caveat is that the sources in Federman et al. (2023) were more distant (~ 400 pc) and therefore had

a maximum recoverable scale in their ACA observations of ~ 8000 au, which is $\sim 2.6 \times$ greater than our MRS. Therefore, they would be more sensitive to extremely extended envelope emission. In addition, their observing wavelength is slightly shorter than ours (difference of $\sim 7\%$). The ratio of envelope to disk emission tends to increase at shorter wavelengths (e.g., Cacciapuoti et al. 2023). Conducting a survey similar to that of Federman et al. (2023) in nearby star-forming regions, and possibly including the Total Power Array to increase the MRS, would provide a better benchmark for the GY 91 observations.

While we do not observe unambiguous envelope emission in the molecular lines, our preferential targeting of transitions with $E_u > 25$ K may be biased against detecting colder envelope material. A challenge with observing many of the conventional envelope tracers, such as ^{12}CO , is the severe cloud contamination (Antilen et al. 2023). However, observing SO as a tracer of accretion shocks may offer an indirect probe of envelope infall (e.g., Sakai et al. 2014).

A large fraction of Class I disks identified as having substructures, including GY 91, are located in the Ophiuchus star-forming region (e.g., Sheehan & Eisner 2017, 2018; Segura-Cox et al. 2020; Hsieh et al. 2025; Vioque et al. 2025). McClure et al. (2010) noted that the high extinction in Ophiuchus makes evolutionary classifications more challenging compared to other nearby star-forming regions such as Taurus. In some cases, the embedded nature of Class I disks in Ophiuchus with substructures, such as Oph IRS 63, has been well-characterized by spatially resolved molecular line observations tracing infalling streamer and envelope material (e.g., Podio et al. 2024). High quality molecular line observations of other Ophiuchus sources will be key for confirming their evolutionary status and determining how common substructures are in embedded disks.

7.4. Identifying good probes of disk emission for highly extincted systems

While targeting a severely cloud-contaminated source introduces complications in our analysis, it also provides insights into good tracers of disk properties in highly extinguished YSOs. Given that a large fraction of protoplanetary disks show evidence of cloud contamination, especially those in Ophiuchus (e.g., Reboussin et al. 2015), identifying tracers with minimal cloud contamination is useful for enabling studies of a broader cross-section of disks.

Among the lines firmly detected in the GY 91 disk, $\text{CS } J = 6 - 5$, $\text{N}_2\text{H}^+ J = 3 - 2$, and $\text{H}_2\text{CS } 8_{1,7} - 7_{1,6}$ appear to have minimal cloud contamination. The

targeted CS and H₂CS transitions have relatively high E_u values (49.3 and 73.4 K, respectively), so they are expected to preferentially trace warm disk gas over cold foreground cloud material. In addition, N₂H⁺ and CS are common dense gas tracers due to their high critical densities (e.g., Shirley 2015), so they are expected to be better at tracing denser disk gas compared to more diffuse cloud material.

We observe severe cloud contamination in H₂CO 4_{0,4}-3_{0,3} and C¹⁸O, but are still able to distinguish disk emission due to the cloud contamination mostly being limited to one side of the disk. We observed no cloud contamination, but also little disk emission, from H₂CO 4_{2,3}-3_{2,2}. The faint H₂CO 4_{2,3}-3_{2,2} line has a much higher E_u (82 K) compared to the heavily cloud-contaminated H₂CO 4_{0,4}-3_{0,3} line (34.9 K). Targeting an H₂CO line with an E_u between these two values may be better suited for probing disk emission in extinguished sources. ¹³C¹⁸O shows no cloud contamination, but also only marginal disk emission at best. Targeting the 3 – 2 transition of C¹⁷O, which is less abundant than C¹⁸O but more abundant than ¹³C¹⁸O, may strike the right balance between being abundant enough to be readily detectable in the disk but not so abundant that cloud emission becomes significant. CO isotopologue transitions with higher upper state energy levels may also be useful to target, but have more stringent weather requirements.

CO isotopologues have commonly been used to estimate dynamical stellar masses (e.g. Simon et al. 2000; Braun et al. 2021). Our observations show that for systems where CO isotopologues are not a good option for tracing disk kinematics due to severe cloud contamination, CS 6 – 5 can be an effective dynamical stellar mass probe.

8. CONCLUSIONS

We present new ALMA Band 7 molecular line and continuum observations to study the physical and chemical properties of the Class I YSO GY 91. Our new observations of GY 91 help to provide a roadmap for more accurate characterizations of the physical and chemical properties of disks in highly extinguished environments. Our main results are as follows:

- We obtained strong detections ($>10\sigma$) of CS, N₂H⁺, C¹⁸O, H₂CO 4_{0,4}-3_{0,3}, and H₂CS, a weak detection ($>5\sigma$) of H₂CO 4_{2,3}-3_{2,2}, and a tentative detection of ¹³C¹⁸O.
- Observations of CS and N₂H⁺ show kinematics consistent with Keplerian disk rotation and minimal cloud contamination, while H₂CO 4_{0,4}-3_{0,3}

and C¹⁸O show significant cloud emission at velocities blue-shifted with respect to the systemic velocity.

- The CS and H₂CS radial profiles are similar, both peaking around ~ 25 au and flattening out past 150 au. N₂H⁺ shows a more extended profile with a peak further out at ~ 50 au. Outside the dust continuum, we also observed an intensity change that may be indicative of ringed substructure in H₂CO 4_{0,4}-3_{0,3} and possibly C¹⁸O at a radius of around 200 au. Whereas the continuum emission appears to be largely axisymmetric, we observe azimuthal asymmetries in CS and H₂CS emission, with brighter emission in the southeast.
- By modeling CS kinematics, we inferred a dynamical stellar mass of $0.58 M_{\odot}$. This mass is higher than previous estimates based on stellar evolution models ($0.25 M_{\odot}$), falling in line with previous findings that the dynamical masses of late M stars can be significantly larger than estimates from evolutionary models.
- Disk masses were estimated using both MCFOST dust continuum radiative transfer modeling ($M_{\text{gas}} = 0.013 M_{\odot}$, given a dust mass of $44 M_{\oplus}$ and gas-to-dust ratio of 100) and comparisons of N₂H⁺ and C¹⁸O fluxes to literature thermochemical models ($M_{\text{gas}} = 0.008 M_{\odot}$). Both values are consistent with expectations for a gravitationally stable disk ($M_{\text{disk}} < 0.06 M_{\odot}$), given a stellar mass of $0.6 M_{\odot}$.
- Comparisons of our ACA and 12-m continuum observations show similar fluxes, suggesting that the dust emission is dominated by the disk rather than by envelope emission. Our molecular lines do not exhibit clear evidence of envelope emission, although the species and transitions chosen may not be optimal for tracing envelope emission, and cloud contamination may obscure envelope emission. We recommend further observations to examine the evolutionary status of GY 91 in order to clarify the timescales of the onset of disk substructures.

ACKNOWLEDGMENTS

We thank the anonymous referee for comments improving the clarity of the manuscript. This paper makes use of the following ALMA data: ADS/JAO.ALMA#2021.1.01588.S and

#2018.1.00028.S. ALMA is a partnership of ESO (representing its member states), NSF (USA) and NINS (Japan), together with NRC (Canada), MOST and ASIAA (Taiwan), and KASI (Republic of Korea), in cooperation with the Republic of Chile. The Joint ALMA Observatory is operated by ESO, AUI/NRAO and NAOJ. We thank Ryan Loomis for serving as our contact scientist, Patrick Sheehan for assisting with the observing proposal, and Alice Booth and Adolfo Carvalho for helpful discussions. J.H. and S.D.J acknowledge support from the National Science Foundation under Grant No. AST-2307916. S.D.J. also acknowledges support from the National Science Foundation Graduate Research Fellowship under Grant No. DGE-2437839. R.L.G. acknowledges funding from the French Agence Nationale de la Recherche (ANR) through the project MAPSAJE (ANR-24-CE31-2126-01). F.M. acknowledges funding from the European Research Council (ERC) under the European Union’s Horizon Europe research and innovation program (grant agreement No. 101053020, project Dust2Planets). Support for C.J.L. was provided by NASA through the NASA Hubble Fellowship grant No. HST-HF2-51535.001-A awarded by the Space Telescope Science Institute, which is operated by the Association of Universities for Research in Astronomy, Inc., for

NASA, under contract NAS5-26555. Support for F.L. was provided by NASA through the NASA Hubble Fellowship grant #HST-HF2-51512.001-A awarded by the Space Telescope Science Institute, which is operated by the Association of Universities for Research in Astronomy, Incorporated, under NASA contract NAS5-26555S. This research has made use of NASA’s Astrophysics Data System Bibliographic Services and the SIMBAD database, operated at CDS, Strasbourg, France.

Facilities: ALMA

Software: AstroPy (Astropy Collaboration et al. 2013, 2018, 2022); analysisUtils (Hunter et al. 2023), bettermoments (Teague & Foreman-Mackey 2018; Teague 2019b), CASA (CASA Team et al. 2022); DiskJockey (Czekala et al. 2015); dsharp-opac (Birnstiel et al. 2018) eddy (Teague 2019c); emcee (Foreman-Mackey et al. 2013); FERIA (Oya et al. 2022); gofish (Teague 2019a); matplotlib (Hunter 2007); MCFOST (Pinte et al. 2006, 2009), MPol (Czekala et al. 2023; Zawadzki et al. 2023); NumPy (Harris et al. 2020); pymcfost (<https://github.com/cpinte/pymcfost>); pyro (Bingham et al. 2019); RADMC3D (Dullemond 2012); VISIBLE (Loomis et al. 2018); visread (Czekala et al. 2021)

APPENDIX

A. CHANNEL MAPS

Channel maps for all detected lines are shown in Figure A.1.

Fig. Set GY 91 channel maps

B. MATCHED FILTERING ANALYSIS

We applied matched filtering with the VISIBLE package (Loomis et al. 2018) to quantify the line detection significance. VISIBLE creates a set of visibilities from an input template line cube and then cross-correlates them with the observed spectral line visibilities to assess how well they match. Initial imaging of CS showed high S/N emission with a Keplerian rotation signature consistent with a disk origin. We thus used the CASA-generated CLEAN model image cube as the template, since other molecules originating in the disk should have a similar kinematic pattern. The visibility weights were renormalized based on channel ranges where no line emission was expected. The matched filter responses for all targeted lines (besides CS) are shown in Figure B.1. Nearly all lines are detected at $> 5\sigma$, except for the $^{13}\text{C}^{18}\text{O}$ line, which is tentatively detected at the 4.5σ level. For H_2CO $J = 4_{0,4}-3_{0,3}$ and C^{18}O , the impulse response peaks at a slightly lower velocity than the systemic velocity we measure from CS in Section 4. We attribute this shift in the impulse response to cloud contamination in H_2CO and C^{18}O , which is blueshifted relative to the disk systemic velocity.

C. INFERRING THE DISK ORIENTATION

Sheehan & Eisner (2018) inferred an inclination of $41^\circ \pm 1^\circ$ from radiative transfer modeling of $870\ \mu\text{m}$ continuum observations, while Cieza et al. (2021) inferred an inclination of $32^\circ.5 \pm 0^\circ.4$ by searching for the combination of P.A. and inclination that minimizes the scatter of the deprojected visibilities from high-resolution 1.3 mm continuum observations. Given the disagreement in the literature, we used MPoL (Zawadzki et al. 2023; Czekala et al. 2023) to

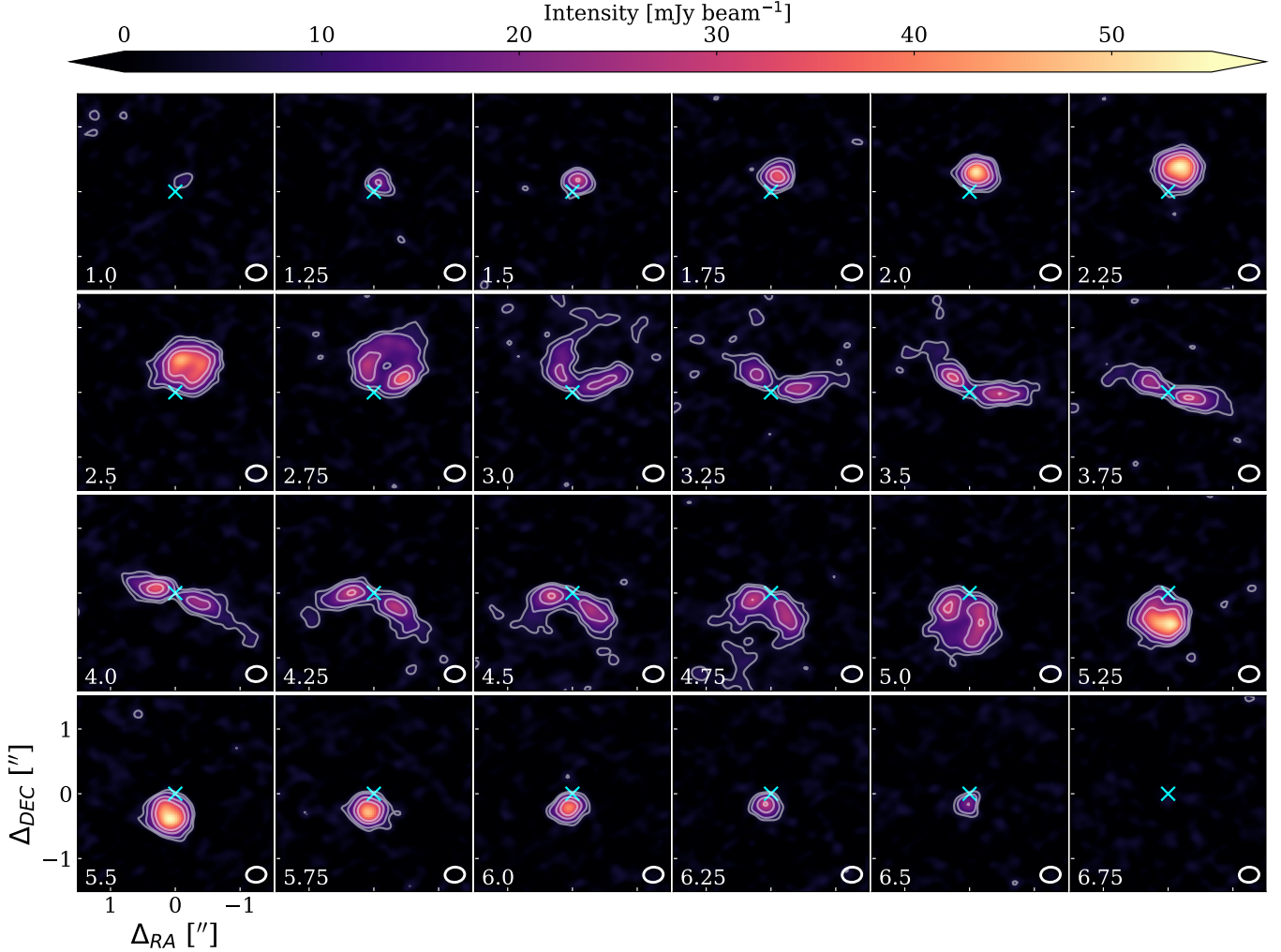


Figure A.1. CS channel maps. The LSRK velocity (km s^{-1}) is labeled in the bottom left corner of each panel. Contours correspond to 3, 5, 10, and 15σ , where σ is the rms listed in Table 3. The synthesized beam size is shown in the bottom right corner. The cyan cross marks the position of the continuum peak. The complete figure set (7 images) is available in the online journal.

perform parametric modeling of the continuum observations from Cieza et al. (2021), which are the highest-resolution observations available.

The raw data were retrieved from program 2018.1.00028.S (PI: L. Cieza) via the ALMA archive and calibrated with the CASA 5.4 pipeline. Details of the observations are described in Cieza et al. (2021). We flagged channels where ^{12}CO emission was expected and averaged the remaining channels to produce continuum-only visibilities. We applied two rounds of phase self-calibration, the first with a scan-length solution interval and the second with a 360 s solution interval. Because the absolute weights of ALMA measurement sets are known to be sometimes incorrect (see, e.g., Zawadzki et al. 2023), we used the `visread` package (Czekala et al. 2021) to rescale the weights.

To infer the inclination, we modeled the disk with the following radial intensity profile:

$$I(r) = A_0 \exp\left(-\frac{r^2}{2\sigma_0^2}\right) + \sum_{i=1}^5 A_i \exp\left(-\frac{(r - r_i)^2}{2\sigma_i^2}\right), \quad (\text{C1})$$

MPoL was used to generate a model image for a given set of phase center offsets (Δx in the east-west and Δy in the north-south directions), inclination, and P.A. and then to generate visibilities from the model image at the same uv points as the data. Thus, the model has 21 free parameters. The source distance was fixed to 140 pc. Priors

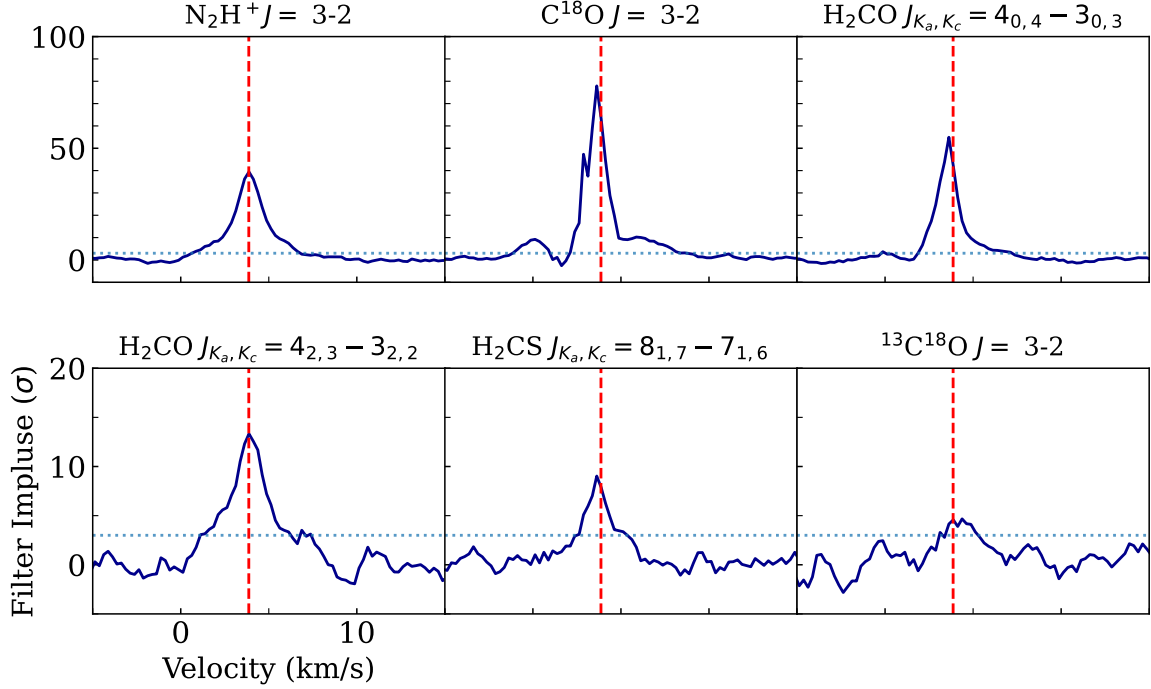


Figure B.1. Matched filter response spectrum for all lines besides CS, using the CS CLEAN model as a template. The blue line indicates the 3σ impulse response level. The red dashed line corresponds to the systemic velocity (3.87 km s^{-1})

were set based on the ring properties presented in Cieza et al. (2021). The stochastic variational inference (SVI) algorithm (Hoffman et al. 2013) implementation in `pyro` (Bingham et al. 2019) was used to estimate the posterior under the assumption that it is approximately a multivariate normal distribution. We ran SVI for 15,000 iterations and assessed convergence based on the evidence lower bound (ELBO). We then drew 2000 samples from the posterior in order to calculate the medians and 68% confidence intervals for the model parameters, which are listed in Table 9. Figure C.1 compares the CLEAN images, residuals, and radial profiles of the observations and model, showing that the observations are reproduced well.

We then used the MPoL model results to estimate R_{90} , the radius that encloses 90% of the disk flux. For each set of samples from the posteriors, we first calculated the radial intensity profile $I(r)$, computed the cumulative flux for a series of radial bins up to several hundred au, where the cumulative flux leveled out, and finally calculated R_{90} . Taking the median and standard deviation of the R_{90} results for all radial profiles, we estimate that $R_{90} = 117 \pm 1 \text{ au}$.

REFERENCES

Anderson, D. E., Blake, G. A., Bergin, E. A., et al. 2019, *ApJ*, 881, 127, doi: [10.3847/1538-4357/ab2cb5](https://doi.org/10.3847/1538-4357/ab2cb5)

Andrews, S. M., Huang, J., Pérez, L. M., et al. 2018, *ApJL*, 869, L41, doi: [10.3847/2041-8213/aaf741](https://doi.org/10.3847/2041-8213/aaf741)

Antilen, J., Casassus, S., Cieza, L. A., & González-Ruiz, C. 2023, *MNRAS*, 522, 2611, doi: [10.1093/mnras/stad975](https://doi.org/10.1093/mnras/stad975)

Astropy Collaboration, Robitaille, T. P., Tollerud, E. J., et al. 2013, *A&A*, 558, A33, doi: [10.1051/0004-6361/201322068](https://doi.org/10.1051/0004-6361/201322068)

Astropy Collaboration, Price-Whelan, A. M., Sipőcz, B. M., et al. 2018, *AJ*, 156, 123, doi: [10.3847/1538-3881/aa8c4f](https://doi.org/10.3847/1538-3881/aa8c4f)

Astropy Collaboration, Price-Whelan, A. M., Lim, P. L., et al. 2022, *ApJ*, 935, 167, doi: [10.3847/1538-4357/ac7c74](https://doi.org/10.3847/1538-4357/ac7c74)

Baraffe, I., Homeier, D., Allard, F., & Chabrier, G. 2015, *A&A*, 577, A42, doi: [10.1051/0004-6361/201425481](https://doi.org/10.1051/0004-6361/201425481)

Baruteau, C., Crida, A., Paardekooper, S. J., et al. 2014, in *Protostars and Planets VI*, ed. H. Beuther, R. S. Klessen, C. P. Dullemond, & T. Henning, 667–689, doi: [10.2458/azu_uapress_9780816531240-ch029](https://doi.org/10.2458/azu_uapress_9780816531240-ch029)

Bingham, E., Chen, J. P., Jankowiak, M., et al. 2019, *Journal of Machine Learning Research*, 20, 1, <http://jmlr.org/papers/v20/18-403.html>

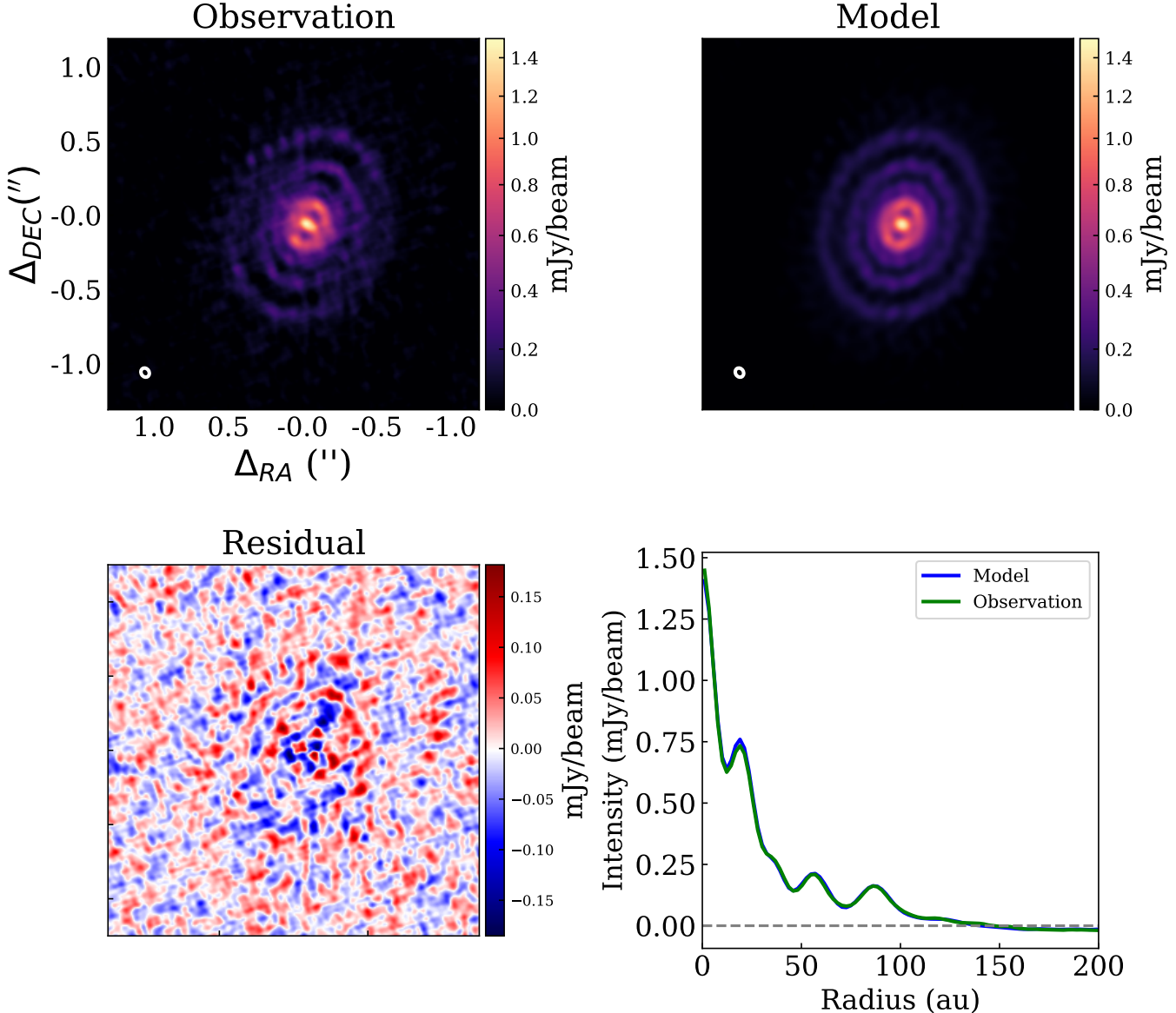


Figure C.1. Top left: 1.3 millimeter dust continuum observations from Cieza et al. (2021). The beam size is indicated in the lower left corner. Top right: CLEAN image of best-fit `pyro` model. Bottom left: Residual image made from subtracting model visibilities from data. Bottom right: Comparison of the observed and model radial profiles generated from the CLEAN images.

Birnstiel, T., Dullemond, C. P., Zhu, Z., et al. 2018, *ApJL*, 869, L45, doi: [10.3847/2041-8213/aaf743](https://doi.org/10.3847/2041-8213/aaf743)

Bisschop, S. E., Jørgensen, J. K., Bourke, T. L., Bottinelli, S., & van Dishoeck, E. F. 2008, *A&A*, 488, 959, doi: [10.1051/0004-6361:200809673](https://doi.org/10.1051/0004-6361:200809673)

Braun, T. A. M., Yen, H.-W., Koch, P. M., et al. 2021, *ApJ*, 908, 46, doi: [10.3847/1538-4357/abd24f](https://doi.org/10.3847/1538-4357/abd24f)

Briggs, D. S. 1995, PhD thesis, New Mexico Institute of Mining and Technology

Bruderer, S. 2013, *A&A*, 559, A46, doi: [10.1051/0004-6361/201321171](https://doi.org/10.1051/0004-6361/201321171)

Bruderer, S., van Dishoeck, E. F., Doty, S. D., & Herczeg, G. J. 2012, *A&A*, 541, A91, doi: [10.1051/0004-6361/201118218](https://doi.org/10.1051/0004-6361/201118218)

Butner, H. M., Natta, A., & Evans, II, N. J. 1994, *ApJ*, 420, 326, doi: [10.1086/173562](https://doi.org/10.1086/173562)

Cacciapuoti, L., Macias, E., Maury, A. J., et al. 2023, *A&A*, 676, A4, doi: [10.1051/0004-6361/202346204](https://doi.org/10.1051/0004-6361/202346204)

Cacciapuoti, L., Testi, L., Maury, A. J., et al. 2025, *A&A*, 700, A188, doi: [10.1051/0004-6361/202554645](https://doi.org/10.1051/0004-6361/202554645)

Calahan, J. K., Bergin, E. A., Bosman, A. D., et al. 2023, *Nature Astronomy*, 7, 49, doi: [10.1038/s41550-022-01831-8](https://doi.org/10.1038/s41550-022-01831-8)

Table 9. Parameter inferences for `pyro` continuum intensity model

Parameter	Priors	Value
Δx (arcsec)	Norm(0.0, 0.003)	-0.0333 ± 0.0005
Δy (arcsec)	Norm(0.0, 0.003)	-0.0646 ± 0.0004
Position angle (deg) ^a	Norm(160.0, 10.0)	157.6 ± 0.5
Inclination (deg)	Norm(40.0, 10.0)	36.4 ± 0.3
$\log(A_0/\text{Jy arcsec}^{-1})$	Norm(0.0, 0.3)	$-0.115^{+0.008}_{-0.009}$
$\log(\sigma_0/\text{au})$	Norm(0.7, 0.1)	0.663 ± 0.007
r_1 (au)	Norm(21, 10)	20.24 ± 0.07
$\log(A_1/\text{Jy arcsec}^{-1})$	Norm(-1.0, 0.5)	$-0.551^{+0.005}_{-0.004}$
$\log(\sigma_1/\text{au})$	Norm(0.8, 0.3)	0.644 ± 0.007
r_2 (au)	Norm(38, 10)	36.9 ± 0.1
$\log(A_2/\text{Jy arcsec}^{-1})$	Norm(-1.0, 0.5)	-0.97 ± 0.01
$\log(\sigma_2/\text{au})$	Norm(0.8, 0.3)	0.6 ± 0.1
r_3 (au)	Norm(58, 10)	56.8 ± 0.1
$\log(A_3/\text{Jy arcsec}^{-1})$	Norm(-1.0, 0.5)	-1.127 ± 0.008
$\log(\sigma_3/\text{au})$	Norm(0.8, 0.3)	0.78 ± 0.01
r_4 (au)	Norm(88, 10)	85.3 ± 0.2
$\log(A_4/\text{Jy arcsec}^{-1})$	Norm(-1.0, 0.5)	-1.37 ± 0.01
$\log(\sigma_4/\text{au})$	Norm(0.8, 0.3)	0.87 ± 0.02
r_5 (au)	Norm(105, 10)	104 ± 2
$\log(A_5/\text{Jy arcsec}^{-1})$	Norm(0.8, 0.3)	$-1.87^{+0.01}_{-0.02}$
$\log(\sigma_5/\text{au})$	Norm(0.7, 0.1)	1.40 ± 0.02

^aDefined to be east of north

Cánovas, H., Cantero, C., Cieza, L., et al. 2019, *A&A*, 626, A80, doi: [10.1051/0004-6361/201935321](https://doi.org/10.1051/0004-6361/201935321)

Carney, M. T., Hogerheijde, M. R., Loomis, R. A., et al. 2017, *A&A*, 605, A21, doi: [10.1051/0004-6361/201629342](https://doi.org/10.1051/0004-6361/201629342)

CASA Team, Bean, B., Bhatnagar, S., et al. 2022, *PASP*, 134, 114501, doi: [10.1088/1538-3873/ac9642](https://doi.org/10.1088/1538-3873/ac9642)

Chiang, E. I., & Goldreich, P. 1997, *ApJ*, 490, 368, doi: [10.1086/304869](https://doi.org/10.1086/304869)

Choi, J., Dotter, A., Conroy, C., et al. 2016, *ApJ*, 823, 102, doi: [10.3847/0004-637X/823/2/102](https://doi.org/10.3847/0004-637X/823/2/102)

Cieza, L. A., Ruíz-Rodríguez, D., Hales, A., et al. 2019, *MNRAS*, 482, 698, doi: [10.1093/mnras/sty2653](https://doi.org/10.1093/mnras/sty2653)

Cieza, L. A., González-Ruiz, C., Hales, A. S., et al. 2021, *MNRAS*, 501, 2934, doi: [10.1093/mnras/staa3787](https://doi.org/10.1093/mnras/staa3787)

Cleeves, L. I., Bergin, E. A., & Harries, T. J. 2015, *ApJ*, 807, 2, doi: [10.1088/0004-637X/807/1/2](https://doi.org/10.1088/0004-637X/807/1/2)

Czekala, I., Andrews, S. M., Jensen, E. L. N., et al. 2015, *ApJ*, 806, 154, doi: [10.1088/0004-637X/806/2/154](https://doi.org/10.1088/0004-637X/806/2/154)

Czekala, I., Loomis, R., Andrews, S., Huang, J., & Rosenfeld, K. 2021, MPoL-dev/visread, v0.0.1, Zenodo, doi: [10.5281/zenodo.4432501](https://doi.org/10.5281/zenodo.4432501)

Czekala, I., Andrews, S. M., Torres, G., et al. 2017, *ApJ*, 851, 132, doi: [10.3847/1538-4357/aa9be7](https://doi.org/10.3847/1538-4357/aa9be7)

Czekala, I., Jennings, J., Zawadzki, B., et al. 2023, MPoL-dev/MPoL: v0.2.0 Release, v0.2.0, Zenodo, doi: [10.5281/zenodo.3594081](https://doi.org/10.5281/zenodo.3594081)

D'Alessio, P., Calvet, N., & Hartmann, L. 1997, *ApJ*, 474, 397, doi: [10.1086/303433](https://doi.org/10.1086/303433)

D'Alessio, P., Cantö, J., Calvet, N., & Lizano, S. 1998, *ApJ*, 500, 411, doi: [10.1086/305702](https://doi.org/10.1086/305702)

de Geus, E. J., Bronfman, L., & Thaddeus, P. 1990, *A&A*, 231, 137

Doppmann, G. W., Greene, T. P., Covey, K. R., & Lada, C. J. 2005, *AJ*, 130, 1145, doi: [10.1086/431954](https://doi.org/10.1086/431954)

Dotter, A. 2016, *ApJS*, 222, 8, doi: [10.3847/0067-0049/222/1/8](https://doi.org/10.3847/0067-0049/222/1/8)

Draine, B. T. 2003, *ARA&A*, 41, 241, doi: [10.1146/annurev.astro.41.011802.094840](https://doi.org/10.1146/annurev.astro.41.011802.094840)

Dullemond, C. P. 2012, RADMC-3D: A multi-purpose radiative transfer tool, *Astrophysics Source Code Library*. <http://ascl.net/1202.015>

Endres, C. P., Schlemmer, S., Schilke, P., Stutzki, J., & Müller, H. S. P. 2016, *Journal of Molecular Spectroscopy*, 327, 95, doi: [10.1016/j.jms.2016.03.005](https://doi.org/10.1016/j.jms.2016.03.005)

Enoch, M. L., Evans, Neal J., I., Sargent, A. I., & Glenn, J. 2009, *ApJ*, 692, 973, doi: [10.1088/0004-637X/692/2/973](https://doi.org/10.1088/0004-637X/692/2/973)

Facchini, S., Teague, R., Bae, J., et al. 2021, AJ, 162, 99, doi: [10.3847/1538-3881/abf0a4](https://doi.org/10.3847/1538-3881/abf0a4)

Federman, S., Megeath, S. T., Tobin, J. J., et al. 2023, ApJ, 944, 49, doi: [10.3847/1538-4357/ac9f4b](https://doi.org/10.3847/1538-4357/ac9f4b)

Foreman-Mackey, D., Hogg, D. W., Lang, D., & Goodman, J. 2013, Publications of the Astronomical Society of the Pacific, 125, 306, doi: [10.1086/670067](https://doi.org/10.1086/670067)

Gaia Collaboration, Prusti, T., de Bruijne, J. H. J., et al. 2016, A&A, 595, A1, doi: [10.1051/0004-6361/201629272](https://doi.org/10.1051/0004-6361/201629272)

Gaia Collaboration, Brown, A. G. A., Vallenari, A., et al. 2021, A&A, 649, A1, doi: [10.1051/0004-6361/202039657](https://doi.org/10.1051/0004-6361/202039657)

Garufi, A., Podio, L., Codella, C., et al. 2021, A&A, 645, A145, doi: [10.1051/0004-6361/202039483](https://doi.org/10.1051/0004-6361/202039483)

Gelman, A., Carlin, J. B., Stern, H. S., et al. 2014, Bayesian Data Analysis

Ginski, C., Facchini, S., Huang, J., et al. 2021, ApJL, 908, L25, doi: [10.3847/2041-8213/abdf57](https://doi.org/10.3847/2041-8213/abdf57)

Goldreich, P., & Lynden-Bell, D. 1965, MNRAS, 130, 125, doi: [10.1093/mnras/130.2.125](https://doi.org/10.1093/mnras/130.2.125)

Goldreich, P., & Tremaine, S. 1980, ApJ, 241, 425, doi: [10.1086/158356](https://doi.org/10.1086/158356)

Goldsmith, P. F., & Langer, W. D. 1999, ApJ, 517, 209, doi: [10.1086/307195](https://doi.org/10.1086/307195)

Gross, R. E., & Cleeves, L. I. 2025, ApJ, 980, 189, doi: [10.3847/1538-4357/ada939](https://doi.org/10.3847/1538-4357/ada939)

Guerra-Alvarado, O. M., Carrasco-González, C., Macías, E., et al. 2024, A&A, 686, A298, doi: [10.1051/0004-6361/202349046](https://doi.org/10.1051/0004-6361/202349046)

Guzmán, V. V., Öberg, K. I., Carpenter, J., et al. 2018, ApJ, 864, 170, doi: [10.3847/1538-4357/aad778](https://doi.org/10.3847/1538-4357/aad778)

Guzmán, V. V., Bergner, J. B., Law, C. J., et al. 2021, ApJS, 257, 6, doi: [10.3847/1538-4365/ac1440](https://doi.org/10.3847/1538-4365/ac1440)

Harris, C. R., Millman, K. J., van der Walt, S. J., et al. 2020, Nature, 585, 357, doi: [10.1038/s41586-020-2649-2](https://doi.org/10.1038/s41586-020-2649-2)

Henning, T., & Stognienko, R. 1996, A&A, 311, 291

Hildebrand, R. H. 1983, QJRAS, 24, 267

Hiraoka, K., Ohashi, N., Kihara, Y., et al. 1994, Chemical Physics Letters, 229, 408, doi: [10.1016/0009-2614\(94\)01066-8](https://doi.org/10.1016/0009-2614(94)01066-8)

Hoffman, M. D., Blei, D. M., Wang, C., & Paisley, J. 2013, J. Mach. Learn. Res., 14, 1303–1347

Hsieh, C.-H., Arce, H. G., Maureira, M. J., et al. 2024, ApJ, 973, 138, doi: [10.3847/1538-4357/ad6152](https://doi.org/10.3847/1538-4357/ad6152)

Hsieh, C.-H., Arce, H. G., José Maureira, M., et al. 2025, arXiv e-prints, arXiv:2504.11577, doi: [10.48550/arXiv.2504.11577](https://doi.org/10.48550/arXiv.2504.11577)

Huang, J., Bergin, E. A., Le Gal, R., et al. 2024, ApJ, 973, 135, doi: [10.3847/1538-4357/ad6447](https://doi.org/10.3847/1538-4357/ad6447)

Huang, J., Andrews, S. M., Dullemond, C. P., et al. 2018, ApJL, 869, L42, doi: [10.3847/2041-8213/aaf740](https://doi.org/10.3847/2041-8213/aaf740)

Hunter, J. D. 2007, Computing in Science and Engineering, 9, 90, doi: [10.1109/MCSE.2007.55](https://doi.org/10.1109/MCSE.2007.55)

Hunter, T. R., Petry, D., Barkats, D., Corder, S., & Indebetouw, R. 2023, analysisUtils, 2.6, Zenodo, Zenodo, doi: [10.5281/zenodo.7502160](https://doi.org/10.5281/zenodo.7502160)

Kepley, A. A., Tsutsumi, T., Brogan, C. L., et al. 2020, PASP, 132, 024505, doi: [10.1088/1538-3873/ab5e14](https://doi.org/10.1088/1538-3873/ab5e14)

Keppler, M., Teague, R., Bae, J., et al. 2019, A&A, 625, A118, doi: [10.1051/0004-6361/201935034](https://doi.org/10.1051/0004-6361/201935034)

Keyte, L., Kama, M., Booth, A. S., et al. 2023, Nature Astronomy, 7, 684, doi: [10.1038/s41550-023-01951-9](https://doi.org/10.1038/s41550-023-01951-9)

Kratter, K., & Lodato, G. 2016, ARA&A, 54, 271, doi: [10.1146/annurev-astro-081915-023307](https://doi.org/10.1146/annurev-astro-081915-023307)

Lauer, T. R., Ajhar, E. A., Byun, Y. I., et al. 1995, AJ, 110, 2622, doi: [10.1086/117719](https://doi.org/10.1086/117719)

Law, C. J., Loomis, R. A., Teague, R., et al. 2021, ApJS, 257, 3, doi: [10.3847/1538-4365/ac1434](https://doi.org/10.3847/1538-4365/ac1434)

Le Gal, R., Öberg, K. I., Loomis, R. A., Pegues, J., & Bergner, J. B. 2019, ApJ, 876, 72, doi: [10.3847/1538-4357/ab1416](https://doi.org/10.3847/1538-4357/ab1416)

Le Gal, R., Öberg, K. I., Teague, R., et al. 2021, ApJS, 257, 12, doi: [10.3847/1538-4365/ac2583](https://doi.org/10.3847/1538-4365/ac2583)

Long, F., Pinilla, P., Herczeg, G. J., et al. 2018, ApJ, 869, 17, doi: [10.3847/1538-4357/aae8e1](https://doi.org/10.3847/1538-4357/aae8e1)

Loomis, R. A., Cleeves, L. I., Öberg, K. I., Guzman, V. V., & Andrews, S. M. 2015, ApJL, 809, L25, doi: [10.1088/2041-8205/809/2/L25](https://doi.org/10.1088/2041-8205/809/2/L25)

Loomis, R. A., Öberg, K. I., Andrews, S. M., et al. 2018, AJ, 155, 182, doi: [10.3847/1538-3881/aab604](https://doi.org/10.3847/1538-3881/aab604)

Loomis, R. A., Facchini, S., Benisty, M., et al. 2025, ApJL, 984, L7, doi: [10.3847/2041-8213/adc43a](https://doi.org/10.3847/2041-8213/adc43a)

Macías, E., Guerra-Alvarado, O., Carrasco-González, C., et al. 2021, A&A, 648, A33, doi: [10.1051/0004-6361/202039812](https://doi.org/10.1051/0004-6361/202039812)

Mathis, J. S., Rumpl, W., & Nordsieck, K. H. 1977, ApJ, 217, 425, doi: [10.1086/155591](https://doi.org/10.1086/155591)

McClure, M. K., Furlan, E., Manoj, P., et al. 2010, ApJS, 188, 75, doi: [10.1088/0067-0049/188/1/75](https://doi.org/10.1088/0067-0049/188/1/75)

Morbidelli, A. 2020, A&A, 638, A1, doi: [10.1051/0004-6361/202037983](https://doi.org/10.1051/0004-6361/202037983)

Müller, H. S. P., Schlöder, F., Stutzki, J., & Winnewisser, G. 2005, Journal of Molecular Structure, 742, 215, doi: [10.1016/j.molstruc.2005.01.027](https://doi.org/10.1016/j.molstruc.2005.01.027)

Müller, H. S. P., Thorwirth, S., Roth, D. A., & Winnewisser, G. 2001, A&A, 370, L49, doi: [10.1051/0004-6361:20010367](https://doi.org/10.1051/0004-6361:20010367)

Öberg, K. I., Guzmán, V. V., Walsh, C., et al. 2021, ApJS, 257, 1, doi: [10.3847/1538-4365/ac1432](https://doi.org/10.3847/1538-4365/ac1432)

Ohashi, N., Tobin, J. J., Jørgensen, J. K., et al. 2023, ApJ, 951, 8, doi: [10.3847/1538-4357/acd384](https://doi.org/10.3847/1538-4357/acd384)

Oya, Y., Kibukawa, H., Miyake, S., & Yamamoto, S. 2022, *PASP*, 134, 094301, doi: [10.1088/1538-3873/ac8839](https://doi.org/10.1088/1538-3873/ac8839)

Paardekooper, S., Dong, R., Duffell, P., et al. 2023, in *Astronomical Society of the Pacific Conference Series*, Vol. 534, *Protostars and Planets VII*, ed. S. Inutsuka, Y. Aikawa, T. Muto, K. Tomida, & M. Tamura, 685, doi: [10.48550/arXiv.2203.09595](https://doi.org/10.48550/arXiv.2203.09595)

Paneque-Carreño, T., Pérez, L. M., Benisty, M., et al. 2021, *ApJ*, 914, 88, doi: [10.3847/1538-4357/abf243](https://doi.org/10.3847/1538-4357/abf243)

Paxton, B., Bildsten, L., Dotter, A., et al. 2011, *ApJS*, 192, 3, doi: [10.1088/0067-0049/192/1/3](https://doi.org/10.1088/0067-0049/192/1/3)

Pegues, J., Öberg, K. I., Bergner, J. B., et al. 2020, *ApJ*, 890, 142, doi: [10.3847/1538-4357/ab64d9](https://doi.org/10.3847/1538-4357/ab64d9)

Pegues, J., Czekala, I., Andrews, S. M., et al. 2021, *ApJ*, 908, 42, doi: [10.3847/1538-4357/abd4eb](https://doi.org/10.3847/1538-4357/abd4eb)

Pineda, J. E., Arzoumanian, D., Andre, P., et al. 2023, in *Astronomical Society of the Pacific Conference Series*, Vol. 534, *Protostars and Planets VII*, ed. S. Inutsuka, Y. Aikawa, T. Muto, K. Tomida, & M. Tamura, 233, doi: [10.48550/arXiv.2205.03935](https://doi.org/10.48550/arXiv.2205.03935)

Pinte, C., Harries, T. J., Min, M., et al. 2009, *A&A*, 498, 967, doi: [10.1051/0004-6361/200811555](https://doi.org/10.1051/0004-6361/200811555)

Pinte, C., Ménard, F., Duchêne, G., & Bastien, P. 2006, *A&A*, 459, 797, doi: [10.1051/0004-6361:20053275](https://doi.org/10.1051/0004-6361:20053275)

Podio, L., Ceccarelli, C., Codella, C., et al. 2024, *A&A*, 688, L22, doi: [10.1051/0004-6361/202450742](https://doi.org/10.1051/0004-6361/202450742)

Qi, C., Öberg, K. I., Wilner, D. J., et al. 2013, *Science*, 341, 630, doi: [10.1126/science.1239560](https://doi.org/10.1126/science.1239560)

Qi, C., Öberg, K. I., Espaillat, C. C., et al. 2019, *ApJ*, 882, 160, doi: [10.3847/1538-4357/ab35d3](https://doi.org/10.3847/1538-4357/ab35d3)

Reboussin, L., Guilloteau, S., Simon, M., et al. 2015, *A&A*, 578, A31, doi: [10.1051/0004-6361/201525705](https://doi.org/10.1051/0004-6361/201525705)

Ricci, L., Testi, L., Natta, A., et al. 2010, *A&A*, 512, A15, doi: [10.1051/0004-6361/200913403](https://doi.org/10.1051/0004-6361/200913403)

Rosenfeld, K. A., Andrews, S. M., Wilner, D. J., & Stempels, H. C. 2012, *ApJ*, 759, 119, doi: [10.1088/0004-637X/759/2/119](https://doi.org/10.1088/0004-637X/759/2/119)

Sakai, N., Sakai, T., Hirota, T., et al. 2014, *Nature*, 507, 78, doi: [10.1038/nature13000](https://doi.org/10.1038/nature13000)

Segura-Cox, D. M., Schmiedeke, A., Pineda, J. E., et al. 2020, *Nature*, 586, 228, doi: [10.1038/s41586-020-2779-6](https://doi.org/10.1038/s41586-020-2779-6)

Sheehan, P. D., & Eisner, J. A. 2017, *ApJL*, 840, L12, doi: [10.3847/2041-8213/aa6df8](https://doi.org/10.3847/2041-8213/aa6df8)

—. 2018, *ApJ*, 857, 18, doi: [10.3847/1538-4357/aaae65](https://doi.org/10.3847/1538-4357/aaae65)

Shirley, Y. L. 2015, *PASP*, 127, 299, doi: [10.1086/680342](https://doi.org/10.1086/680342)

Simon, M., Dutrey, A., & Guilloteau, S. 2000, *ApJ*, 545, 1034, doi: [10.1086/317838](https://doi.org/10.1086/317838)

Suriano, S. S., Li, Z.-Y., Krasnopolsky, R., & Shang, H. 2018, *MNRAS*, 477, 1239, doi: [10.1093/mnras/sty717](https://doi.org/10.1093/mnras/sty717)

Takahashi, S. Z., & Inutsuka, S.-i. 2014, *ApJ*, 794, 55, doi: [10.1088/0004-637X/794/1/55](https://doi.org/10.1088/0004-637X/794/1/55)

Taniguchi, K., Pineda, J. E., Caselli, P., et al. 2024, *ApJ*, 965, 162, doi: [10.3847/1538-4357/ad2fa1](https://doi.org/10.3847/1538-4357/ad2fa1)

Tanious, M., Le Gal, R., Neri, R., et al. 2024, *A&A*, 687, A92, doi: [10.1051/0004-6361/202348785](https://doi.org/10.1051/0004-6361/202348785)

Teague, R. 2019a, *The Journal of Open Source Software*, 4, 1632, doi: [10.21105/joss.01632](https://doi.org/10.21105/joss.01632)

—. 2019b, *Research Notes of the American Astronomical Society*, 3, 74, doi: [10.3847/2515-5172/ab2125](https://doi.org/10.3847/2515-5172/ab2125)

—. 2019c, *The Journal of Open Source Software*, 4, 1220, doi: [10.21105/joss.01220](https://doi.org/10.21105/joss.01220)

—. 2020, *richteague/keplerian_mask*: Initial Release, 1.0, Zenodo, doi: [10.5281/zenodo.4321137](https://doi.org/10.5281/zenodo.4321137)

Teague, R., & Foreman-Mackey, D. 2018, *bettermoments*: A robust method to measure line centroids, v1.0, Zenodo, doi: [10.5281/zenodo.1419754](https://doi.org/10.5281/zenodo.1419754)

Terwisscha van Scheltinga, J., Hogerheijde, M. R., Cleeves, L. I., et al. 2021, *ApJ*, 906, 111, doi: [10.3847/1538-4357/abc9ba](https://doi.org/10.3847/1538-4357/abc9ba)

Trapman, L., Zhang, K., van't Hoff, M. L. R., Hogerheijde, M. R., & Bergin, E. A. 2022, *ApJL*, 926, L2, doi: [10.3847/2041-8213/ac4f47](https://doi.org/10.3847/2041-8213/ac4f47)

Trapman, L., Longarini, C., Rosotti, G. P., et al. 2025a, *ApJL*, 984, L18, doi: [10.3847/2041-8213/adc430](https://doi.org/10.3847/2041-8213/adc430)

Trapman, L., Zhang, K., Rosotti, G. P., et al. 2025b, *arXiv e-prints*, arXiv:2506.10738, doi: [10.48550/arXiv.2506.10738](https://doi.org/10.48550/arXiv.2506.10738)

Tripathi, A., Andrews, S. M., Birnstiel, T., & Wilner, D. J. 2017, *ApJ*, 845, 44, doi: [10.3847/1538-4357/aa7c62](https://doi.org/10.3847/1538-4357/aa7c62)

Valdivia-Mena, M. T., Pineda, J. E., Segura-Cox, D. M., et al. 2022, *A&A*, 667, A12, doi: [10.1051/0004-6361/202243310](https://doi.org/10.1051/0004-6361/202243310)

van der Plas, G., Casassus, S., Ménard, F., et al. 2014, *ApJL*, 792, L25, doi: [10.1088/2041-8205/792/2/L25](https://doi.org/10.1088/2041-8205/792/2/L25)

van Kempen, T. A., van Dishoeck, E. F., Brinch, C., & Hogerheijde, M. R. 2007, *A&A*, 461, 983, doi: [10.1051/0004-6361:20065174](https://doi.org/10.1051/0004-6361:20065174)

van't Hoff, M. L. R., Walsh, C., Kama, M., Facchini, S., & van Dishoeck, E. F. 2017, *A&A*, 599, A101, doi: [10.1051/0004-6361/201629452](https://doi.org/10.1051/0004-6361/201629452)

Vioque, M., Kurovic, N. T., Trapman, L., et al. 2025, *ApJ*, 989, 9, doi: [10.3847/1538-4357/adc7b0](https://doi.org/10.3847/1538-4357/adc7b0)

Warren, S. G., & Brandt, R. E. 2008, *Journal of Geophysical Research (Atmospheres)*, 113, D14220, doi: [10.1029/2007JD009744](https://doi.org/10.1029/2007JD009744)

Zawadzki, B., Czekala, I., Loomis, R. A., et al. 2023, *PASP*, 135, 064503, doi: [10.1088/1538-3873/acdf84](https://doi.org/10.1088/1538-3873/acdf84)

Zhang, K., Blake, G. A., & Bergin, E. A. 2015, *ApJL*, 806, L7, doi: [10.1088/2041-8205/806/1/L7](https://doi.org/10.1088/2041-8205/806/1/L7)

Zhang, K., Booth, A. S., Law, C. J., et al. 2021, ApJS, 257, 5, doi: [10.3847/1538-4365/ac1580](https://doi.org/10.3847/1538-4365/ac1580)

Zhang, S., Zhu, Z., Huang, J., et al. 2018, ApJL, 869, L47, doi: [10.3847/2041-8213/aaf744](https://doi.org/10.3847/2041-8213/aaf744)